Progress in Materials Science 54 (2009) 839–873

Contents lists available at ScienceDirect

Progress in Materials Science

journal homepage: www.elsevier.com/locate/pmatsci

Microtwinning and other shearing mechanisms at intermediate temperatures in Ni-based superalloys

L. Kovarik [a,*], R.R. Unocic [a], Ju Li [b], P. Sarosi [c], C. Shen [d], Y. Wang [a], M.J. Mills [a]

[a] Department of Materials Science and Engineering, The Ohio State University, 2041 College Road, Columbus, OH 43210, USA
[b] Department of Materials Science and Engineering, University of Pennsylvania, 3231 Walnut Street, Philadelphia, PA 19104, USA
[c] General Motors Research and Development Center, Warren, MI 48090, USA
[d] GE Global Research, Niskayuna, NY 12309, USA

ARTICLE INFO

ABSTRACT

In Ni-based superalloys, microtwinning is observed as an important deformation mechanism at intermediate temperature and low stress and strain rate conditions. Current knowledge concerning this unusual deformation mode is comprehensively reviewed, and fundamental aspects of the process are further developed using state of the art experimental and modeling techniques. The nature of microtwins and the microtwinning dislocations at the atomic level have been determined using High Angle Annular Dark Field Scanning Transmission Electron Microscopy imaging. The results unambiguously confirm that the operative twinning dislocations are identical Shockley partials $a/6\langle 1\,1\,2\rangle$, and that they propagate through the γ' precipitates in closely-separated pairs on consecutive $\{1\,1\,1\}$ planes. The rate-limiting process of the microtwinning deformation mechanism is the diffusion-controlled reordering in γ'-phase. It is shown that reordering requires very simple, vacancy-mediated exchange between Al and Ni atoms. The energetic aspect of the vacancy-mediated exchanges is studied for the first time using ab initio calculations. The concept of reordering as a rate-limiting process is generalized and shown to be relevant for other, previously reported deformation mechanisms in superalloys such as $a\langle 1\,1\,2\rangle$ dislocation ribbons, and superlattice intrinsic and superlattice extrinsic stacking fault formation. Other diffusion phenomena associated with microtwinning, such as segregation of heavy elements, is also discussed and supported by experimental evidence. The influence of the γ/γ' microstructure

* Corresponding author.
E-mail address: kovarik.8@osu.edu (L. Kovarik).

0079-6425/$ - see front matter
doi:10.1016/j.pmatsci.2009.03.010

on microtwinning deformation mode is also discussed in light of observations and phase-field dislocation modeling results.

Contents

1. Introduction

Nickel base superalloys are an important class of materials that are used in demanding high temperature structural applications such as the hot zone of aircraft gas turbine engines due to their highly desirable material properties such as high temperature strength and their resistance to creep, thermal/mechanical fatigue and oxidation. These unique properties are attributed to alloy chemistry and microstructure, which consists primarily of ordered, Ni_3Al-based, $L1_2$-structured, γ′ precipitates that are coherently embedded in a solid solution γ matrix. Dependent upon how the material is processed and heat-treated, precipitate size, size distribution and spacing can be tailored for optimal mechanical properties. It is the size of these microstructural features that will ultimately control the microscopic deformation mode and macroscopic deformation response.

High temperature deformation mechanisms of polycrystalline superalloys have been extensively studied in the past. These studies have uncovered a variety of different deformation mechanisms that can become operative depending on the testing temperature, applied stress and microstructure. At lower temperatures and higher stresses, shearing of the γ′ precipitates occurs via the coupled movement of paired $a/2\langle 1\,1\,0\rangle$ dislocations. These are perfect dislocations in the matrix, and when coupled together by an anti-phase boundary (APB) in the γ′-phase, they can also shear the precipitates without leaving a planar fault in their wake [1–3]. A recent summary of this mechanism and its use in modeling the yield strength in polycrystalline alloys, in combination with other strengthening mechanisms such as grain boundary and solid solution strengthening, has been presented by Kozar et al. [4]. This mechanism appears to prevail up to around 600 °C in polycrystalline alloys. At

much higher temperatures (around 800 °C), climb by-pass of γ′ precipitates by individual, unpaired $a/2\langle 1\,1\,0\rangle$ dislocations is predominant [5]. We note that this mechanism forms the basis of several well-established creep models for particle and precipitate strengthened alloys [6,7]. With respect to disk applications; however, this climb by-pass regime appears to be well beyond the practical service temperatures.

Several other mechanisms have been identified in the temperature range between APB shearing and climb by-pass processes. These mechanisms are distinctive in that several types of planar defects are formed in the γ′ precipitates and/or the matrix. It is emphasized that this temperature regime appears to correspond to the onset of more strongly thermally-activated deformation, and is essential to understand with respect to improving the temperature capability of the polycrystalline superalloys. There are several reports of γ′ precipitate shearing modes and the formation of either superlattice intrinsic stacking faults (SISF) and superlattice extrinsic stacking faults (SESF), while $a/2\langle 1\,1\,0\rangle$ dislocations persist in the matrix [8–11]. These "isolated faulting" mechanisms require dissociation reactions at the matrix precipitate interfaces involving $a/2\langle 1\,1\,0\rangle$ dislocations. Another variant on the "isolated faulting" mode was initially documented by Kear et al. [12] in which $a\langle 1\,1\,2\rangle$ perfect matrix dislocations shear the γ′ particles by forming SISFs and SESFs pairs in the γ′ precipitates. Extended faults have also been reported continuously traversing both matrix and precipitates [8,13,14]. These extended faults are typically on the order of a few micrometers in width. Diffraction contrast analysis indicates that the faults are predominantly extrinsic in nature following tensile creep, although a significant density of intrinsic faults are also observed.

Most remarkably, recent experimental work by Kolbe [15] and Viswanathan et al. [11,16] reported on a rather novel deformation mechanism that operates during exposure to moderate stresses and temperatures in the range of 650–750 °C. This mechanism was denoted as microtwinning due to the fact that it imparts very thin twins (microtwins) on the order of 4–50 atomic planes in the deformed microstructure [17]. The microtwins can be readily identified with the help of conventional and high-resolution TEM imaging. The microtwins shear both the γ-phase and γ′-phase and are commonly seen to traverse entire grains. This process has also been observed in the MC2 single crystal alloy using in situ TEM deformation studies at temperature range 800–850 °C. The observations indicate that the dislocations proceed in viscous glide motion [18]. The microtwinning process, and its possible relationship to the other shearing mechanisms, is the focus of the present paper.

It is noted here that the "intermediate temperature" range of interest, roughly 650–850 °C, is below that explored in many previous studies of creep in single crystal Ni-based superalloys for blade applications [19,20]. The polycrystalline Ni-based superalloys considered presently have been developed to have modest lattice misfit and γ′ volume fractions close to 50%. It is noted that the mechanisms may differ from those observed in the single crystal blade alloys where larger γ′ volume fractions and lattice misfit between the matrix and precipitates create significant internal stresses that make the interfaces even more profound barriers to slip. Nevertheless, as discussed below, important commonality between mechanisms in disk and blade alloys may exist for similar deformation regimes. Indeed many of the important initial studies of the "intermediate temperature" regime have been performed on early "generation" Ni-based superalloys, and these studies are discussed in the context of more recent work on polycrystalline disk alloys.

In Section 2 of this paper, the present status of knowledge concerning microtwinning in Ni-based superalloys is reviewed in detail. In Section 3, new high-resolution imaging of the microtwins and twinning partial dislocations is presented which unambiguously confirms earlier work concerning the nature of the twinning partials. These results are consistent with the hypothesis that thermally-activated microtwinning is controlled by a diffusion-mediated reordering within the γ′ precipitates. In Section 4, a simple model of this process is presented. The detailed process by which reordering may take place is explored using ab initio calculations in Section 5, which results in a quantitative correlation between reordering and Ni self-diffusion. In Section 6, evidence for segregation to stacking faults and microtwins in the γ′-phase are presented and discussed. Finally, in Section 7, the importance of reordering for several of the other deformation mechanisms observed in both disk and blade type alloys is also discussed.

2. Previous experimental evidence for microtwinning at intermediate temperatures

There have been several previous observations of microtwinning following the higher temperature deformation of Ni-based superalloys. These results and proposed mechanisms are briefly summarized, and additional evidence provided by recent high-resolution scanning transmission electron microscopy (HR-STEM) observations are presented.

2.1. Observations of microtwinning after creep of γ/γ' superalloys

There have been several early reports of the occurrence of microtwinning following creep of single crystal and polycrystalline superalloys. Kear et al. [21,22] provided an early evidence for extended stacking faults and deformation twins in Mar-M200 single crystals oriented near [1 1 0] deformation axis. The formation of the microtwins was rationalized in the context of γ' intrinsic stacking faults (SISF) that are commonly observed in the deformed microstructure. It was postulated that a build-up of the faults on consecutive planes will lead to the formation of twins in γ'. As the build-up becomes larger, the array of Shockley partials that are present at the interface will create a high stress configuration. Annihilation of these partials within the γ channels will lead to formation of continuous microtwins. This proposed process of microtwin formation is illustrated in Fig. 1.

Similar reports of microtwins in $\langle 1\,1\,0\rangle$-oriented single crystals of CMSX-4 after relatively low temperature creep (<800 °C) have also been reported by several other groups [23,24]. Ardakani et al. [25] provided one of the most comprehensive studies of microtwinning in the single crystal superalloy, SRR-99 deformed along $\langle 1\,1\,0\rangle$ at 750 °C and 850 MPa. In this study, a range of twin thicknesses were observed via TEM, and the twin volume fraction was observed to increase with increasing strain. Their analysis was the first to show conclusively that twinning contributes significantly to the total creep strain at smaller strain levels. "Embryonic" twins were proposed to arise from the dissociation of $a/2[1\,1\,0]$ matrix dislocations via the reaction:

$$a/2[1\,1\,0] = a/6[1\bar{1}\bar{2}] + a/3[1\,2\,1] \tag{1}$$

This energetically unfavorable dissociation reaction was presumed to be stimulated by the presence of the γ'-phase. As the $a/2[1\,1\,0]$ matrix dislocation encounters a γ' particle, the $a/3[1\,2\,1]$ dislocation could shear the particle, forming an SISF or SESF, but the $a/6[\bar{1}\,\bar{1}\,2]$ partial would be pinned at the entrance side of the particle. This is the case since shearing of the γ' particle by the complete $a/2[1\,1\,0]$ displacement would create a higher energy APB. While not specified in their paper, the twins were presumed to grow by movement of successive $a/3[1\,2\,1]$ partials on adjacent $(1\,\bar{1}\,1)$ planes.

Microtwins were also reported in early work by Guimier and Strudel [26] on the polycrystalline Waspalloy with about 25 volume percent γ' particles. When this same alloy was given a solutionizing heat treatment and quench in order to suppress γ' precipitation, twins were not observed. This sup-

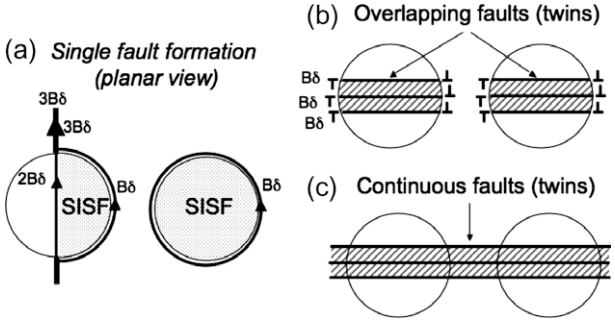

Fig. 1. Proposed mechanism by Kear et al. [21,22] for γ' precipitate shear. (a) A perfect dislocation $a/2[1\,1\,2]$ dissociates into partials at the $\gamma\gamma'$ interface; only the $1/3[1\,1\,2]$ shears the γ'-phase. (b) Overlapping faults are formed and (c) annihilation of the dislocations at the $\gamma\gamma'$ interface, formation of continuous twins.

ports the concept that twinning is related to the presence of the γ′ precipitates, possibly promoting the dissociation reaction (Eq. 1).

2.2. Chen and Knowles mechanism

Knowles and Chen [27] report that SESF configurations in the larger γ′ particles coexist with microtwinning for particular crystal orientations in CMSX-4. The initiation and propagation of the microtwins, as well as the formation of isolated SESFs in the γ′ particles, are presumed to be associated with the operation of two different $a/3\langle 1\,1\,2\rangle$ partials on every {1 1 1} plane (e.g. 2αB then 2αC as shown in Fig. 2a). Passage of the first net 2Dα will create an SESF, while subsequent passages will thicken the twin. For an opposite sense of applied shear stress, an SISF would be expected. The authors make the very interesting observation that microtwins are observed only in orientations for which SESFs are also observed.

The authors propose that the $a/3\langle 1\,1\,2\rangle$ twinning partials arise from a pole mechanism, which originates with the interaction of two identical $a/2\langle 1\,1\,0\rangle$ matrix dislocations (DC), e.g.:

$$a/2[1\,1\,0] + a/2[1\,1\,0] = a[1\,1\,0] = a/3[2\,1\,\bar{1}] + a/3[1\,2\,1] \tag{2}$$

The temperature and stress dependence of the process is associated with the critical size for nucleation of the twin from the pole. Since these are twinning partials of the ordered $L1_2$ structure, the subsequent propagation of the $a/3\langle 1\,1\,2\rangle$ partials is presumably rapid and not rate controlling since the formation of SESF′s and microtwins by this mechanism does not require local diffusion or atomic

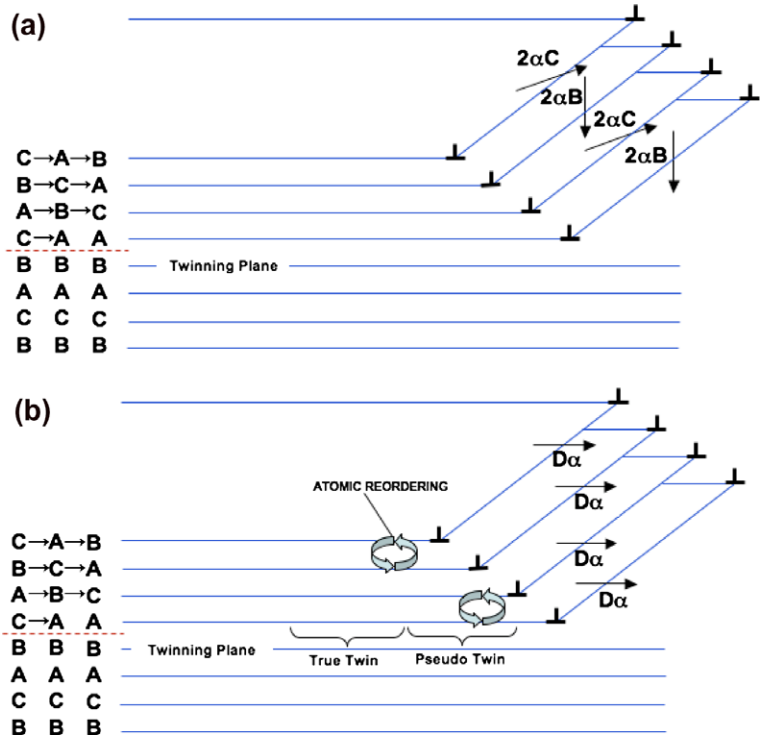

Fig. 2. (a) Model of twin formation by passage of $1/3\langle 1\,1\,2\rangle$ Shockley partials (2αB and 2αC) on adjacent planes. After Chen and Knowles [9]. The four $a/3[1\,1\,2]$ partials create a true-twin in $L1_2$ structure of γ′-phase. (b) Model of twin formation by passage of $1/6\langle 1\,1\,2\rangle$ Shockley partials (Dα) on adjacent planes Kolbe [15]. Thermally-activated reordering is required to create a true-twin in $L1_2$ structure of γ′-phase.

rearrangement. A difficulty with this model for twinning is that it requires successive shear of {1 1 1} planes in directions that are necessarily of small Schmid factor (presuming that the net shear direction, 2Dα, has large Schmid factor).

In this and the earlier models of twinning involving motion of $a/3\langle 1\,1\,2\rangle$ partials, the $L1_2$ lattice of the precipitates would be preserved and "true-twins" would be formed in the precipitates and the matrix. In the next section, we will discuss a novel concept that was introduced by Kolbe et al. [28] proposing a quite different mechanism for the formation of deformation twins in the superalloys.

2.3. Kolbe mechanism for microtwinning and the reordering hypothesis

Kolbe et al. [28] performed in situ TEM deformation experiments at elevated temperature that indicated a distinct transition in deformation mechanism with temperature. Below about 760 °C, dislocation motion was observed to be jerky, in which encounters with γ′ precipitates resulted in distinct waiting times. The shearing dislocations were reported to be $a/2\langle 1\,1\,0\rangle$ type, although no direct evidence was provided to support this claim. In situ deformation at higher temperature gave rise to a distinctly different mode of shearing in which extended faults propagate continuously and viscously through both particles and matrix. These extended faults are associated with partials that move in a correlated manner as pairs. Kolbe [15] hypothesized that these partials may be $a/6\langle 1\,1\,2\rangle$ partials of the same Burgers vector (e.g. a pair of Dα partials), and that they may be traveling on parallel {1 1 1} planes, as illustrated in Fig. 2b. Without detailed confirmation of this hypothesis, Kolbe further deduced that these were in fact microtwins, and that the temperature dependence of the process may be associated with reordering that would ensue in the wake of the twinning $a/6\langle 1\,1\,2\rangle$ partials as they traverse the γ′ particles.

The model of Kolbe is thus differentiated from other studies of microtwinning in the important aspect of the nature of the twinning partial dislocations. Partials of the type $a/3\langle 1\,1\,2\rangle$ preserve the ordering present in the $L1_2$ structure of the precipitates, and consecutive passage of these partials on adjacent {1 1 1} planes would create true-twins in the γ′ particles. In contrast, while the $a/6\langle 1\,1\,2\rangle$ type partials proposed by Kolbe are twinning partials of the FCC matrix, passage of these partials on consecutive {1 1 1} planes in the $L1_2$ structure would create a "pseudo-twin" which would no longer have the $L1_2$ structure. The pseudo-twin would have an orthorhombic structure in which a large number of unfavorable, high-energy nearest neighbor bonds (i.e. Al–Al nearest neighbors in the Ni_3Al structure) would be created. Without presenting concrete supporting evidence, Kolbe proposed that this high-energy structure would not be created, but instead the $L1_2$ structure of the twins in the precipitates would be restored via thermally-activated reordering, as illustrated in Fig. 3 in which four partial dislocations, grouped in pairs, are gliding on consecutive {1 1 1} planes. There are Al–Al nearest neighbors created in the wake of the gliding dislocations, as highlighted with the bonds indicated in the figure.

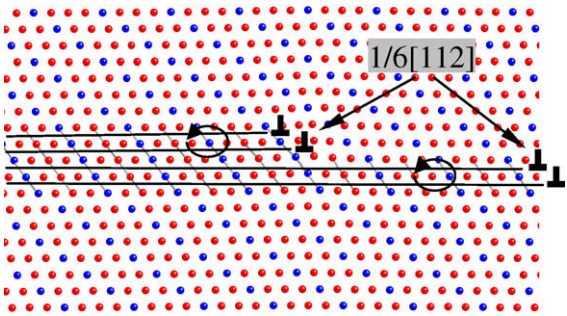

Fig. 3. Schematic of the key aspects of the microtwining deformation mechanism. Shear of γ′-phase is accomplished by a pair of 1/6[1 1 2] partial dislocations. The highlighted Al–Al nearest neighbors can be eliminated by diffusion-mediated reordering, as symbolized by the circular arrows.

In support of this hypothesis is the observation by Kolbe that the partials tended to travel in pairs. A single $a/6\langle 1\ 1\ 2\rangle$ partial would create a complex stacking fault (CSF) in the γ' structure. It is not possible to reorder the Al–Al nearest neighbor bonds at a CSF since any rearrangement of the atoms at the fault would create unfavorable bonds in the adjacent (1 1 1) planes. However, passage of two Shockley partials would create a two-layer CSF that can be reordered into a two-layer superlattice extrinsic stacking fault (SESF). The detailed steps involved in this reordering process are discussed in Section 5.

3. Detailed analysis of microtwins

The hypothesis of Kolbe required validation in several important respects. First and foremost has been to distinguish whether the twinning partials are $a/6\langle 1\ 1\ 2\rangle$ or $a/3\langle 1\ 1\ 2\rangle$ dislocations. Second, is to establish the actual structure of the microtwins in the γ' particles. These analyses have recently been undertaken by Viswanathan et al. [11,16] and Sarosi et al. [29], and the results indicate the twinning partials all have the same Burgers vector and support the claim that the twinning partials are of the $a/6\langle 1\ 1\ 2\rangle$ type. This work has been performed on Rene 88DT deformed in creep at (834 MPa) and 650 °C, and very similar structures have also been found in the alloy Rene 104 deformed at 690 MPa and 677 °C. Under these conditions, microtwinning is the predominant deformation process based on assessment of multiple grains in the TEM specimens. An example of microtwins traversing a grain in

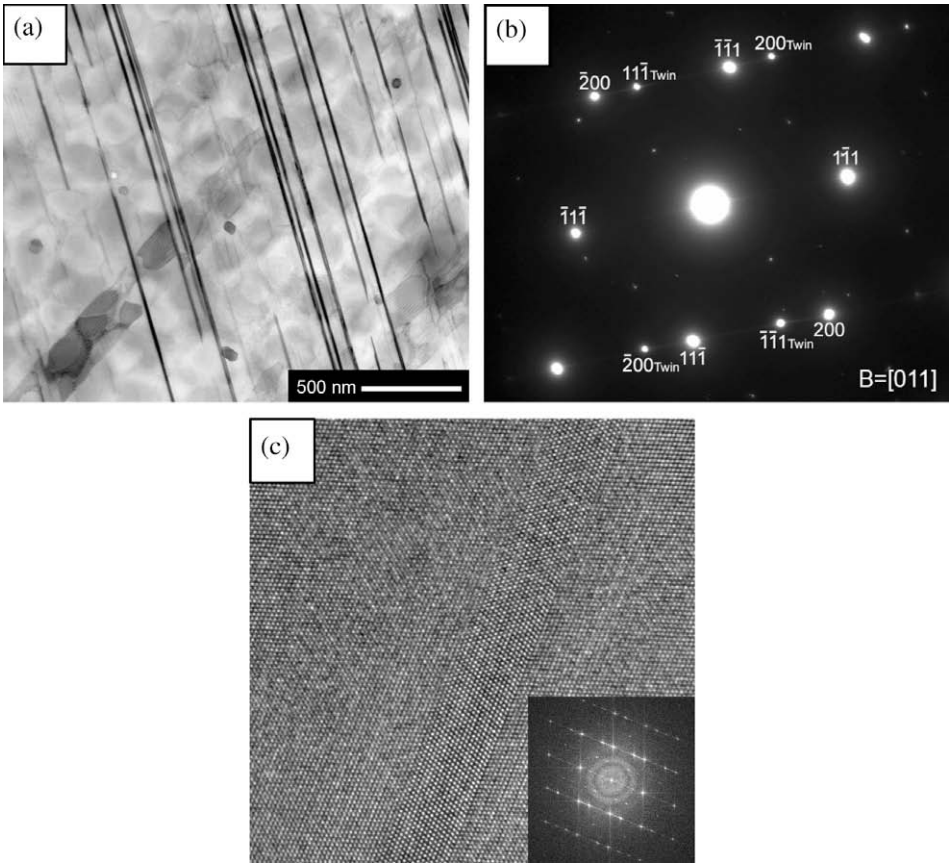

Fig. 4. (a) General view of deformed microstructure revealing microtwins in edge on and inclined orientation. (b) Indexed SADP showing the presence of twin reflections. (c) Microtwin in the γ'-phase that has a thickness of 14 layers. The insert is a Fourier transform confirming the presence of superlattice reflections of the γ'.

Rene 104 is shown in Fig. 4a. The corresponding selected area diffraction pattern showing twin reflections is shown in Fig. 4b.

An example of a high-resolution image of a microtwin stretching across a γ′-precipitate is shown in Fig. 4c. In this particular example the microtwin is 14 layers thick. It is found that a majority of the twins in the γ′-phase have an even number of layers and that their thickness can vary, with most being in the range of 4–50 layers thick [17]. The thickness of the microtwin is defined here by the number of adjacent {1 1 1} planes that have been sheared by partial dislocations. Thus, for example, a four-layer microtwin is formed by propagation of four partial dislocations on four adjacent planes.

This microscopy and diffraction analysis reveals an important aspect regarding the internal structure of the microtwins, that is, the state of order. The two important states that can be distinguished are "true-twin" and "pseudo-twin". In the pseudo-twin configuration, the twinned part of the crystal is structurally a different phase as compared with the $L1_2$ structure. The pseudo-twin has an orthorhombic structure that contains Al–Al nearest neighbors. The pseudo-twin can be distinguished due to the presence of additional diffraction intensities in the electron diffraction patterns. In [1 1 0] zone axis diffraction patterns that contains the twinning plane, the set of {1 1 1} reflections that do not cor-

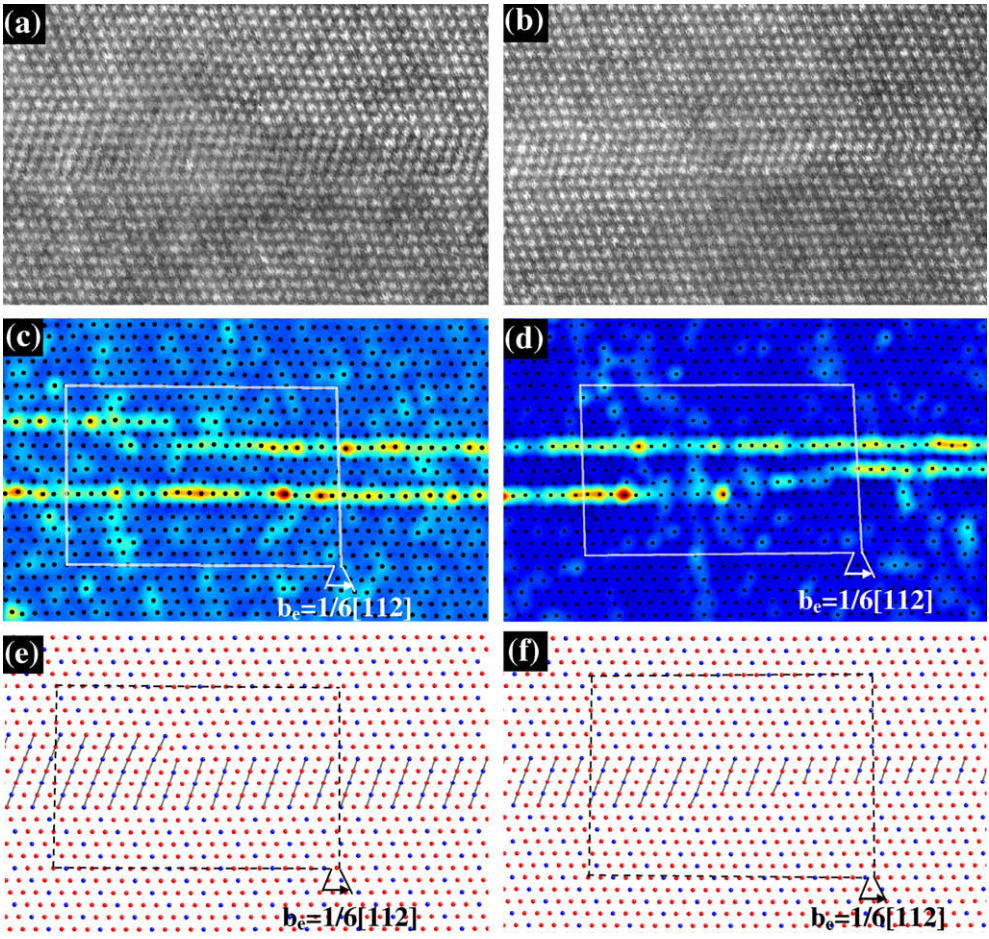

Fig. 5. (a) HAADF image depicting presence of two 30° 1/6[1 1 2] dislocations at the microtwin interface and causing a change in thickness from 4 to 6 layers. (b) HAADF image depicting the presence of two 1/6[1 1 2] dislocations at the microtwin interface, causing a change in thickness from 2 to 4 layers. (c and d) Corresponding RGB colored-coded images based on central symmetry parameter highlighting the interface of the microtwin. (e and f) Simulated structures of the twinned region with two 1/6[1 1 2] dislocations whose Burgers is 30° to the viewing direction (2× 30° 1/6[1 1 2]).

respond to the twinning plane can be used to make this distinction. In a pseudo-twin structure, an intensity peak has to be present at ½ of the $g\{1\ 1\ 1\}$ for two of three possible pseudo-twin variants in the edge-on configuration. These types of reflections have not been observed in any of the analyzed diffraction patterns, which suggest that the microtwins are indeed true-twins.

It should be noted that it is not possible to confirm from a single HRTEM image that the examined microtwin is indeed a "true-twin". This is so because there exists one pseudo-twin variant with apparent mirror plane symmetry in the [1 1 0] examination direction. It is therefore important to have the twinning partial dislocations included in the area of analysis, which unambiguously reveals the type of variant that is present. Detailed discussion on this distinction can be found in Sarosi et al. [29].

The diffraction contrast analyses performed previously to determine the nature of the twinning partials [11] are extremely challenging due to (a) the close separation between some of the partial dislocations, (b) the complicating imaging effect of the γ' particles, (c) the differential thinning of matrix and particles, and (d) the obscuring effect of the faults that are connected to the twinning partials. High-resolution imaging can provide much more definitive conclusions regarding the nature of the twinning partials when compared to diffraction contrast imaging. An example of a microtwin in γ'-phase that contains several twinning dislocations is shown in Fig. 5. These are HAADF STEM images obtained using an FEI Titan 80–300 microscope with c_s-correction on the electron probe operated at 300 kV. This image is taken close to a grain boundary where the microtwin terminated. The HAADF imaging reveals steps due to the twinning partials along the length of the twin. It starts as a two-layer fault and changes to four-layer microtwin in Fig. 5a, and then from 4 to 6 layer microtwin in Fig. 5b.

A better representation of the nature of the microtwins and the partial dislocations can be obtained from color-coded images based on the central/inversion symmetry parameter as shown in Fig. 5c and d. The assignment of the value of the central symmetry was done based on an algorithm implemented in freely available AtomEye visualization software [30]. The center of symmetry color-coding (blue[1] is the symmetry of the perfect crystal, while "warmer" colors represent deviation from the perfect crystal symmetry) enables us to establish that the separation between the Shockley partials is very small, less than 1.5 nm in one case and virtually "compact" in the other case. The high-resolution images also unambiguously confirm that the operative dislocations are Shockley $a/6[1\ 1\ 2]$ partials. The drawing of the Burgers circuit, encompassing the twinned region, reveals that the partial dislocations are two $a/6[1\ 1\ 2]$ dislocations viewed in the 30° orientation. A simulation that depicts the identical displacement and which can be obtained only from two $1/6[1\ 1\ 2]$ dislocations on consecutive planes is shown in Fig. 5e and f. Thus, in this orientation, the $a/6[1\ 1\ 2]$ Shockley partials can be unambiguously distinguished from $a/3[1\ 1\ 2]$ as previously discussed by Sarosi et al. [29].

4. Karthikeyan model for microtwinning

A quantitative model for microtwinning based on Shockley partial shearing process described above, coupled with the necessity for reordering of the twinned regions back to the $L1_2$ structure, has been proposed by Karthikeyan et al. [31]. The model is based upon the assumption that the cooperative movement of the Shockley partial pairs can occur only when the energy of the two-layer fault in its wake is reduced via reordering. Since reordering is a time and temperature dependent process, the twinning partial velocity also has these attributes. The reordering process is assumed to operate within the larger secondary particles, while the tertiary particles are assumed to be small enough to shear athermally. These conditions therefore set upper and lower bounds on the applied shear stress range for which the model is expected to apply. The basic geometry of the model is shown in Fig. 6.

Consider the two-layer fault formed in the wake of the first two Shockley partials. The fault energy of this two-layered pseudo-twin is Γ_{pt}. Reordering reduces the energy of the two-layered fault. If the Shockley partials were to shear the γ' slowly, then there is sufficient time for reordering to take place and the energy penalty is reduced, eventually to that of a true-twin, Γ_{tt}. Karthikeyan et al. [31] assumed that the energy drop takes place exponentially with time such that:

[1] For interpretation of color in Figs. 2, 3, 5, 7–14, 17–20, 22, and 25 the reader is referred to the web version of this article.

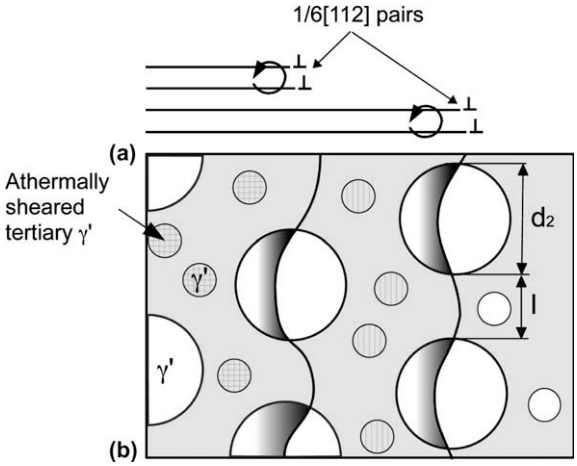

Fig. 6. Schematic illustration of the microtwining mechanism and the geometry of the model. (a) View with the {1 1 1} glide planes "edge-on" and (b) plan view showing the coupled 1/6⟨1 1 2⟩ partials shearing tertiary and secondary γ′. Other quantities are defined in the text.

$$\Gamma(t) = (\Gamma_{pt} - \Gamma_{tt}) \exp(-K \cdot t) + \Gamma_{tt} \tag{3}$$

where K is a constant determining the reordering rate and t is the time. The exponential decay is a statement of the assumption that the pseudo-twin → true-twin transformation is a first-order reaction. The resulting strain rate law based on the Orowan equation is given by:

$$\dot{\gamma} = \rho_{tp} \cdot b_{tp} \cdot v = \rho_{tp} \cdot b_{tp} \frac{D_{ord} \cdot (b_{tp}/x^2)}{\ln\left[f_2 \cdot \Delta\Gamma/(2 \cdot \tau_{eff} \cdot b_{tp} - f_2 \cdot \Gamma_{tt})\right]} \tag{4}$$

where ρ_{tp} is the density of mobile twinning partials, b_{tp} is the Burgers vector of the twinning partial, D_{ord} is the diffusion coefficient for ordering and x is the short range diffusion length (assumed to be several nearest neighbor distances, or $\sim 2 \cdot b$), and f_2 is the volume fraction of the secondary γ′ precipitates. The effective stress, τ_{eff}, in the presence of tertiary γ′ precipitates, is given by:

$$\tau_{eff} = \tau - \frac{f_3 \cdot \Gamma_{pt}}{2 \cdot b_{tp}} \tag{5}$$

The experimental values of parameters such as dislocation density ρ_{tp}, volume fraction of the secondary γ′ precipitate that are critical to the prediction can be determined directly from TEM observations. The magnitude of the strain rate predicted by this model is in good agreement with the observed strain rate [31], particularly for the strain level at which the density of twinning partials has been measured. This agreement suggests that the basic kinetics associated with the twinning partial velocity are reasonable.

In this work, Karthikeyan assumed that D_{ord} could be approximated by the self- diffusion coefficient, and chose the mean value between the diffusion coefficients for Ni and Al for purpose of the initial model evaluation. The validity of this assumption, the exploration of the actual reordering process, and its relationship to self-diffusion has been evaluated by ab initio modeling that will now be presented.

5. Reordering

5.1. Pathways of vacancy reordering

The current high-resolution imaging confirms two important aspect of the theory of microtwinning as previously developed by Kolbe [15] and Viswanathan et al. [11,16]: (a) the operative dislocations

are Shockley partials 1/6[1 1 2] and (b) these partials propagate through γ′ in closely-separated pairs on a consecutive (1 1 1) planes. Images such as Fig. 5a and b enable us to establish that the separation between the Shockley partials is very small, less than 1.5 nm in one case and virtually "compact" in the other case. The small separation suggests that the energy of the section of the microtwin in-between the two partial dislocations must be significantly higher than the energy of the microtwin on either side of the partials. The energy difference of the different sections provides strong energetic counter-balance for the elastic repulsion between the Shockley partials and thus implies that a diffusion-mediated reordering converts the high-energy pseudo-twin on both sides of the dislocations into true-twin (or at least a lower energy) configuration. This suggests that the reordering is happening in the immediate vicinity of the dislocation cores.

Kolbe [15] showed that the pseudo-twins created by an even number of $a/6[1\,1\,2]$ partials could reorder into a true-twin configuration by the process shown in Fig. 7. The scenario considered here is a two-layer microtwin, equivalent to a two-layer CSF. In the vicinity of the two partial dislocations at the right-hand side of the figure, the pseudo-twin is in the as-sheared configuration and contains the Al–Al nearest neighbors as schematically depicted with the grey bonds across the fault planes. The area away from the dislocation at the left-hand side is reordered into a true-twin configuration. According to Kolbe, the reordering can be achieved by a two-step exchange process as shown in Fig. 7a. In the first exchange, Ni and Al atoms are replaced as indicated with the circular arrow 1. The second exchange involves the same Ni atom, but now it replaces another Al atom as shown with the circular arrow 2. The three atoms involved occupy the same (1 1 0) plane, which is perpendicular to the viewing direction. Depiction of the described process from *[1 1̄ 1]* view of the central plane is shown in Fig. 7b. For clarity, only one of the atoms above and below the central plane is shown in this

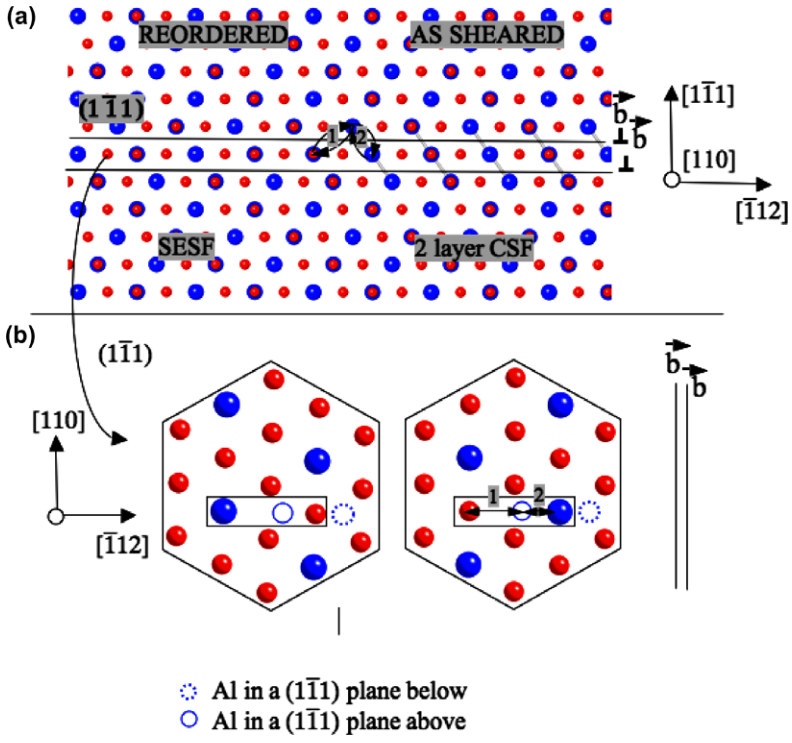

Fig. 7. (a) Two layer fault that has been created by a passage of two $a/6[1\,\bar{1}\,2]$ partial dislocations on consecutive planes, as viewed along the [1 1 0]. The left side of the fault has been reordered and corresponds to SESF. (b) Atomic arrangement in the central plane of SESF and 2CSF. Relative positions of Al atoms in the upper and lower adjacent plane are shown. The atom color-coding is Ni-red "smaller" Al-blue "larger".

projection of the structure. The atoms involved in the exchanges are enclosed in a box. It is important to point out that this proposed process, as well as an alternative path described in [15], do not involve an exchange between nearest neighbors. As a consequence, these reordering paths cannot be accomplished directly by vacancy movement, and are therefore highly unlikely.

Examination of the as-sheared and reordered configurations in Fig. 7 reveals that there is an additional, more direct way for the system to reorder from pseudo- into true-twin configurations. The novel, more direct reordering can be understood from a recognition that the central plane of the faulted structure (central plane in the wake of two $a/6[\bar{1}\,1\,2]$ partial dislocations) consists of a row of anti-site point defects (Al^{Ni} and Ni^{Al}) as shown in Fig. 8a. The anti-site columns are in the close-packed [1 1 0] direction and are perpendicular to the $a/6[\bar{1}\,1\,2]$ Burgers vector. To reorder such a system thus simply requires an exchange between Al and Ni atoms in the anti-site column as shown in Fig. 8b. It should be noted that changing of Al and Ni in any other closed packed ⟨1 1 0⟩ directions would not accomplish reordering into a true-twin configuration as these are not the anti-site columns.

Under the premise that reordering of Ni and Al atoms in a microtwin is a vacancy-mediated diffusion process, one can easily envision several ways in which the vacancy movement can accomplish the swap between Ni and Al sites. For example, in the simplest, most direct and highly correlated case, the vacancy would move in the [1 1 0] anti-site column as shown in Fig. 8c. As the vacancy moves along, the Al and Ni atoms in the column will be placed into the neighboring sites and thus assume positions that are consistent with a true-twin configuration. There are many more viable, but less correlated, vacancy paths that will accomplish the exchange of the Ni and Al sites. One such example is shown in Fig. 8d. In this less correlated movement, the vacancy will enter the mixed column via a Ni^{Al} anti-site, will accomplish one exchange between Al and Ni sites and will exit from the mixed column.

5.2. Ab initio calculations

Understanding the diffusion-mediated reordering mechanism requires quantitative knowledge of the vacancy formation ΔG^{form} and vacancy migration ΔG^{mig} energies associated with a movement

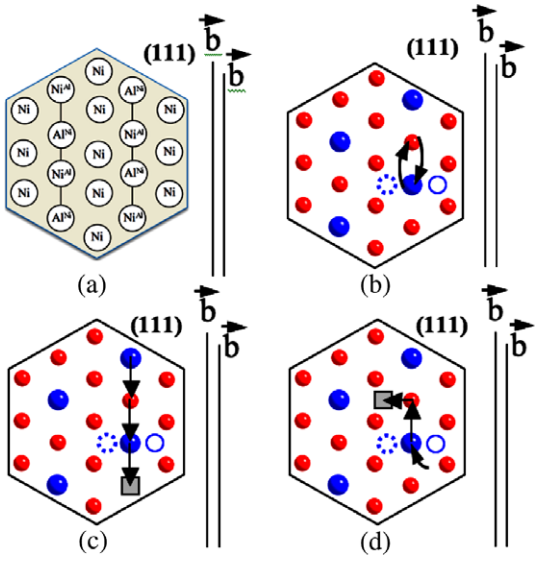

Fig. 8. (a) Schematic of the atom arrangement in the central lane of a two-layer complex fault. (b) Direct exchange of Al and Ni atoms that allow transformation of the "as-sheared" into a "true-twin" configuration. (c) An example of a linear movement of vacancy that enables an exchange between Al and Ni sites in an entire [1 1 0] column. (d) An example of less correlated case that allow single exchange between Al and Ni sites. The atom color-coding is Ni-red "smaller", Al-blue "larger". The grey box represents a vacancy position and the arrows indicate vacancy steps during reordering.

along the viable reordering paths. The values of ΔG^{form} and ΔG^{mig} for the key vacancy exchanges of nickel and aluminum anti-sites have been studied with ab initio calculations. For the purpose of the ab initio calculations described here, the studies were preformed in the context of faulted Ni_3Al super-cell, without considering the stress field of the partial dislocations.

The calculations reported in this work were performed with Vienna Ab initio Simulation Package (VASP) [32–35]. The projector augmented wave (PAW) method in combination with Generalized Gradient Approximation (GGA) for the exchange correlation potential was used [36]. Spin-polarization was considered in the calculations. For the calculation of the migration ΔG^{mig} energies, we used Climbing Image Nudge Elastic Band (NEB) method as implemented in VASP by Henkelman [37]. Five images were used in the NEB calculations. The NEB calculations were performed with *K*-point sampling $1 \times 1 \times 1$ and energy cutoff 270 eV.

The calculations were performed on fully periodic Ni_3Al super-cells that have axes defined by crystallographic directions $3[1\,1\,0]_{Ni3Al} \times [1\,1\,2]_{Ni3Al} \times 7/3[1\,1\,1]_{Ni3Al}$. A two-layer complex stacking fault was introduced into the system by displacing the upper part of the crystal on two consecutive planes by $a/6[1\,1\,2]$. An example of a super-cell with a vacancy on a Ni sub-lattice site in the center of the complex fault (two-layer pseudo-twin) is shown in Fig. 9.

5.3. Energetics of the reordering steps

There are several vacancy pathways that can accomplish the exchange of Ni^{Al} and Al^{Ni} anti-sites. The reordering pathways considered in this work assume that in the start and end point configurations the vacancy is situated on a Ni sub-lattice, unless in the end configuration the vacancy is in the row of anti-sites. In the context of a two-layer complex stacking fault, this means that the vacancy is situated either on a Ni site at the fault interface or a Ni site in the central plane of the fault. The assumption for the vacancy being located on the Ni sub-lattice (Va^{Ni}) stems from previous computational studies that predict a significantly higher concentration of vacancies on Ni sub-lattice for a range of $Ni_{3-x}Al_{1+x}$ stoichiometries ($x \sim \pm 0.1$) [38,39].

The vacancy-mediated exchange of Ni^{Al} and Al^{Ni} can be considered as a minimum three-step jump process. The first step always involves an exchange of a vacancy with an atom in the anti-site [1 1 0] column. Depending upon whether the initial exchange is with Al^{Ni} or Ni^{Al}, the viable pathways can be divided into two main categories.

A schematic representation of the first category, where the jump sequence initiates with Va^{Ni}–Ni^{Al} exchange, is shown in Fig. 10a. Step 1 is an exchange between Va^{Ni} and Ni^{Al}, step 2 is an exchange be-

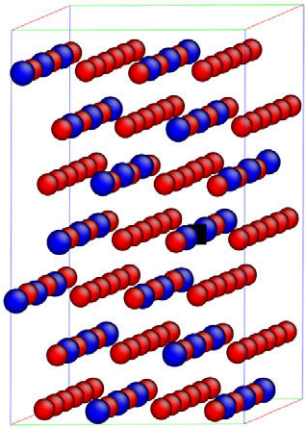

Fig. 9. The super-cell used in the ab initio calculations in near [1 1 0] orientation. The central part of the super-cell contains a two-layer complex stacking fault (CSF). A vacancy is present on a Ni lattice site in the center of the pseudo-twin, as schematically emphasized with the black square. The atom color-coding is Ni-red "smaller", Al-blue "larger".

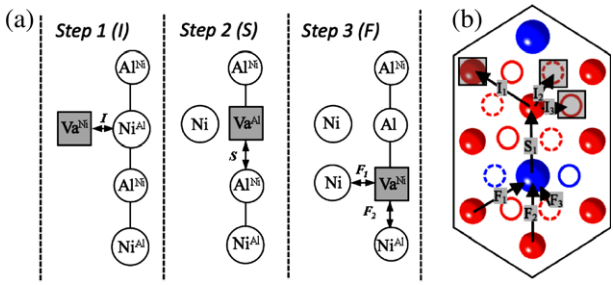

Fig. 10. (a) Schematic of the reordering sequence initiated with an exchange between Va^{Ni} and Ni^{Al}. (b) The actual representation of the atom configuration and the possible reordering pathways. The atom color-coding is Ni-red "smaller", Al-blue "larger".

tween Va^{Al} and Al^{Ni} (places Al on the proper sub-lattice) and step 3 is Va^{Ni}–Ni^{*}, which puts Ni on the proper sub-lattice and thus accomplishes reordering of one Al–Ni pair. The actual representation of the atomic arrangement and the possible sites that can be involved in the exchange are shown in Fig. 10b. There are ten available Va^{Ni} sites for the initial exchange Va^{Al}–Ni^{Al}. Three of the sites are crystallographically unique, labeled as I_1, I_2 and I_3. There are nine Ni sites available for the final exchange, five of which are crystallographically unique. For visual clarity, only three of the five are marked in Fig. 10b as F_1, F_2 and F_3.

An example of the energy landscape for one of the most favorable pathways is shown in Fig. 11a. The individual steps are $I_1S_1F_3$, as referenced in Fig. 10b. The first step I_1 has a migration barrier of 0.93 eV. A similar value for migration energy is obtained for the initial exchange I_2, while the migration barrier associated with exchange I_3 is substantially larger at approximately 1.2 eV. The subsequent exchange S_1 is highly energetically favorable; the system lowers its energy by 0.297 eV. The energetic favorability of S_1 can be ascribed to the fact that one Al–Al nearest bond is eliminated in the system. The migration barrier (ΔG^{mig}) associated with the jump is relatively low, having a value of 0.734 eV. The final step F_3 represents a vacancy exchange with a Ni atom at the interface. This exchange increases the energy of the system by approximately 0.2 eV. The migration barrier associated with the exchange is 0.95 eV. It is important to point out that the exchange F_2, which would allow for linearly-correlated diffusion in the anti-site columns (as described in Fig. 6b), has a migration barrier of approximately 1.2 eV, as seen in Fig. 11b. Therefore, step F_2 is unfavorable. Moreover, the overall energy increase associated with this exchange is approximately 0.4 eV higher than for the F_3 step. From consideration of the possible final steps, the F_2 jump has the highest migration barrier and the highest energy cost, thereby ruling out the linearly-correlated diffusion process.

The second possibility for the reordering jump sequence is initiated with Va^{Ni}–Al^{Ni} exchange. The reordering sequence can involve three steps, as shown in Fig. 12a, four steps as shown in Fig. 12c or any higher number of steps. The reordering paths presented in Fig. 12a and c correspond to a ring-path due to the fact that step 1 creates an Al anti-site which is eliminated in the last step. The actual representation of the atomic arrangement and a three-step path $I_1S_1F_1$ is shown in Fig. 12b. If step 3 would continue in the anti-site row as F_2, the reordering can be envisioned as a process that temporarily creates Al^{Ni} anti-sites due to the first step.

Fig. 13 displays the energy landscape for a jump sequence that corresponds to steps $I_1S_1F_1$ in Fig. 12b. The initial exchange I_1 is highly energetically unfavorable; as a result of this exchange, the energy of the system increases by approximately 0.35 eV. This energy increase can be rationalized by the fact that new Al^{Ni} anti-site is created which shares three Al–Al nearest neighbors. However, the migration barrier (ΔG^{mig}) associated with the exchange is approximately 0.7 eV. Similar values of the energy balance and ΔG^{mig} are obtained for the other possible initial jumps. The second step Va^{Ni}–Ni^{Al} (S_1) also increases the energy of the system. The energy of the system is increased by 0.362 eV. The corresponding migration barrier is approximately $\Delta G^{mig} \sim 1.2$ eV. Only the last step lowers the energy of the system. The energy is lowered by approximately 0.65 eV, which indicates that it is highly energetically favorable. The corresponding migration barrier is only 0.18 eV.

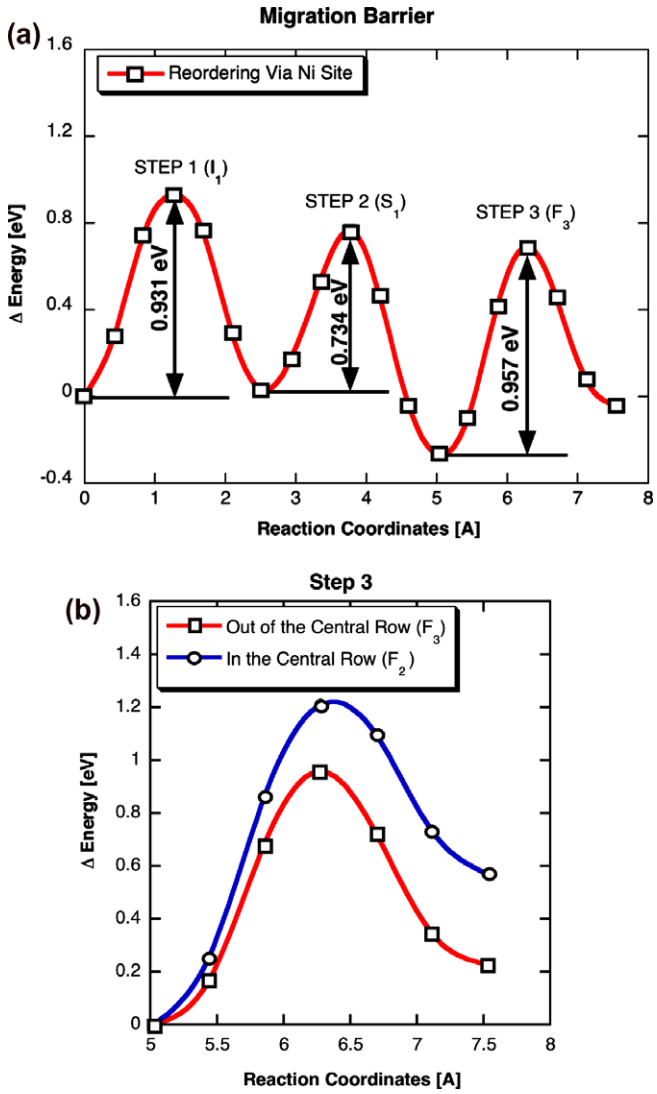

Fig. 11. (a) Energy landscape associated with vacancy steps that accomplish a reordering of single Al–Ni pair. The process initiates with an exchange between Va and Ni. (b) Comparison of the two possible energy barriers for the final exchange (Va^{Ni}–Ni^{Al}) involving either step F_3 (vacancy exchange with an atom at the interface) or step F_2 (linearly-correlated vacancy exchange with a Ni atom in the central plane of the fault).

5.4. Assessment of the reordering pathways

The energy landscape calculations enable us to predict the most likely pathway the vacancy will take in reordering. Based on the presented calculations it becomes evident that the reordering path initiated with the Va^{Ni}–Ni^{Al} exchange will be favored over the path initiated with Va^{Ni}–Al^{Ni}. This is so despite the fact that the migration barrier for the step 1 in the Va^{Ni}–Ni^{Al} exchange is approximately 0.25 eV higher than the step 1 of the Va^{Ni}–Al^{Ni} initiated sequence.

The argument for this conclusion is based on the fact that the reordering sequence initiated with Va^{Ni}–Ni^{Al} exchange has a favorable relation between the forward and backward transition probability

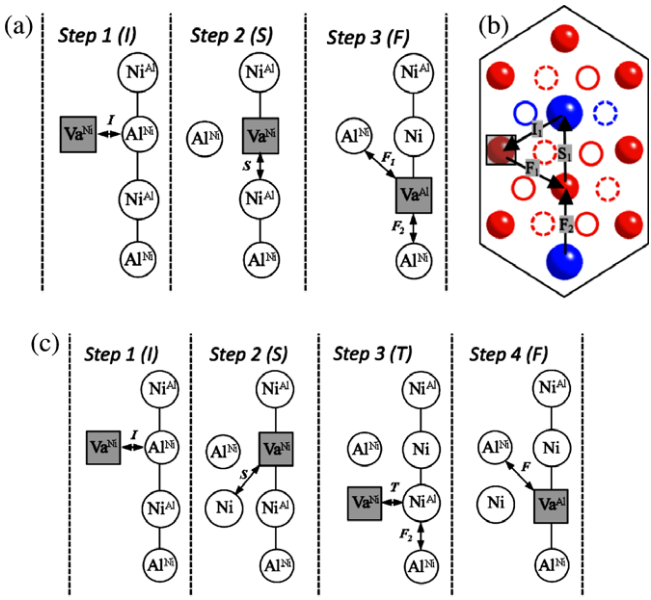

Fig. 12. (a) Three-step reordering sequence that initiates with an exchange between Va^{Ni} and Al^{Ni}. (b) The actual representation of the atom configuration and the possible reordering pathways. The atom color-coding is Ni-red "smaller", Al-blue "larger". (c) Four-step reordering sequence that initiates with an exchange between Va^{Ni} and Al^{Ni}.

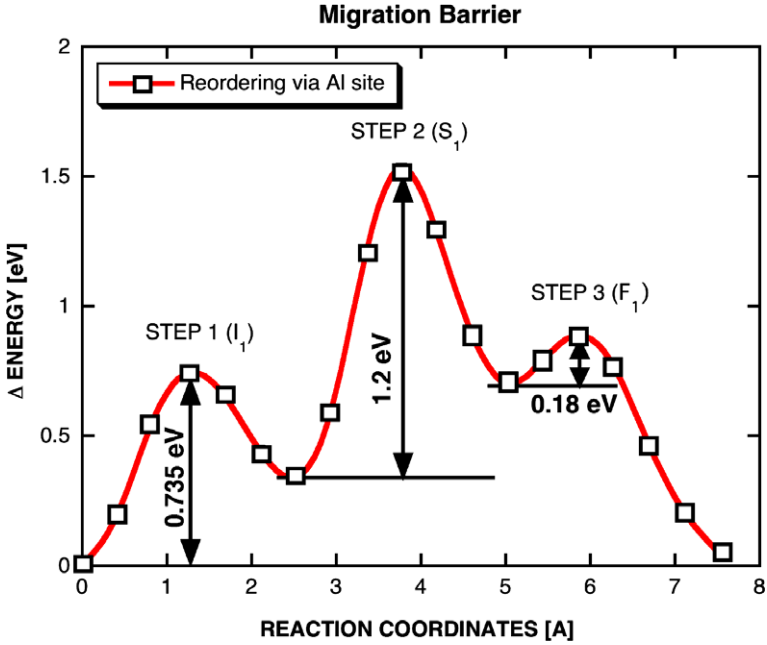

Fig. 13. Energy landscape associated with vacancy steps that accomplish a reordering of single Al–Ni pair. The process initiates with an exchange between Va and Al.

of the involved steps. That is, each step of the sequence has higher transition probability than the previous step backward. This favorable relation guarantees that once the initial exchange has taken place, the next reordering step will be favored.

In comparison, this favorable relation is not found for the reordering sequence initiated with Va^{Ni}–Al^{Ni} exchange. The transition probability for step 2 is very low as compared to the transition probability of the backward step 1. The actual energy barriers are 1.2 eV for the forward (S_1) jump and 0.4 eV for the backward $(\bar{I}_1)$ jump. The difference of 0.8 eV allows us to estimate based on $\Gamma = \nu \cdot \exp\left(\frac{-\Delta G^m}{k_B T}\right)$ that the ratio between transition rates $\bar{I}_1/S_1$ is approximately 14,000 at a temperature of 700 °C, which makes the overall reordering sequence very unlikely.

This analysis indicates that the reordering path initiated with the Va^{Ni}–Ni^{Al} exchange will be dominant. The choice of the last step in the sequence has significant implications for the reordering process as it was shown that the exchange labeled as F_2 would provide a continuous, highly correlated reordering. Due to the fact that the migration barrier associated with this jump F_2 is approximately 0.2 eV higher than the other possible final steps, it can be concluded that the linear, highly correlated motion of vacancy will not be the relevant mode of reordering.

The picture of the reordering process that emerges from these preliminary calculations is the following (see Fig. 14). (a) The vacancy is at the twin interface on Ni site. The most likely reordering jump sequence is such that the vacancy enters the mixed row of the central plane though a Ni site, which enables the subsequent switch with Al. Upon completing this exchange, the vacancy exits from the

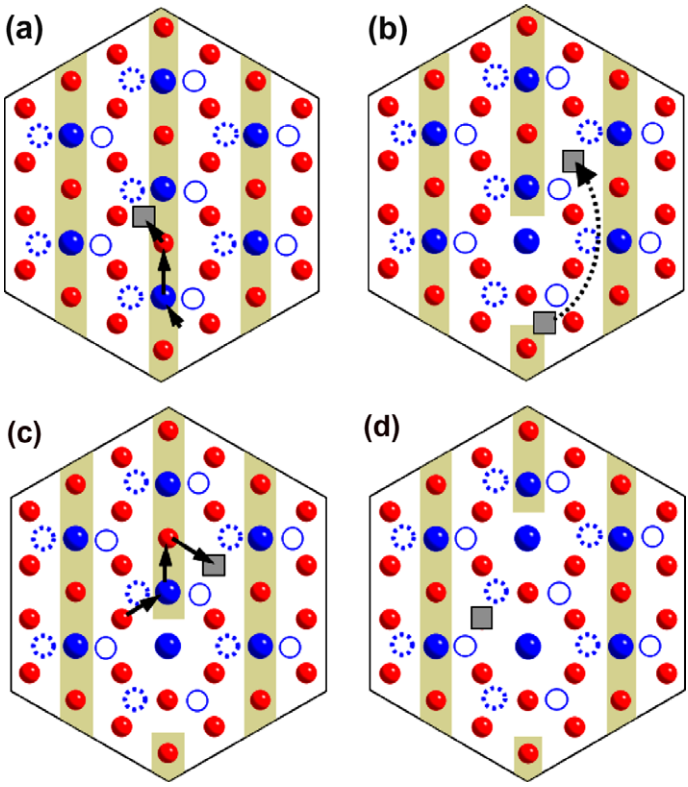

Fig. 14. Sequential picture of the reordering process as deduced from the ab initio analysis. (a) Vacancy (Va^{Ni}) reorders one Al^{Ni}–Ni^{Al} pair through the consecutive jumps in the anti-site column. (b) Vacancy Va^{Ni} diffuses at the interface or its vicinity. (c) Vacancy (Va^{Ni}) enables analogous reordering of Al^{Ni}–Ni^{Al} pair. (d) Vacancy is available for further reordering. Atom color-coding is Ni-red "smaller", Al-blue "larger".

mixed column of the central plane. (b) Following this single pair reordering, it is likely than that the vacancy will stay longer at the interface due to its lower energy of formation in this plane (as discussed in the following section). (c) The process is repeated as the vacancy can participate in a new, analogous reordering process. In the case that the reordering takes place in the vicinity of the previously reordered pair, the energy of the reordering steps is even more favorable. (d) The vacancy is available for further reordering.

5.5. Vacancy formation energy

The vacancy formation energy ΔG^{form} at the Ni sites that serve as the starting point for the reordering was estimated with ab initio calculations. As previously discussed, there exists three crystallographically unique Ni sites from which the reordering sequence can be started. One site is in the central plane and two sites are at the microtwin interface. All three different sites were previously shown in Fig. 10b as being associated with exchanges I_1, I_2 and I_3, respectively.

For an intermetallic compound such as Ni_3Al, the quantity that dictates the concentration of point defects is the effective formation energy ΔG^{form}. The effective formation energy on a Ni site in stoichiometric Ni_3Al can be expressed according to Eq. (6) (the derivation of the equation can be found in the work of Mishin [40,41]). The effective formation energy depends not only on the vacancy formation energy but also on the formation energies of other point defects such as anti-sites as they can transform through appropriate reaction:

$$\Delta H^{\text{form}}_{\text{Va}_{\text{Ni}}} = \varepsilon_{\text{Va}_{\text{Ni}}} + E_0 + \frac{b}{2}(\varepsilon_{Ni_{Al}} - \varepsilon_{Al_{Ni}}) \tag{6}$$

where $\varepsilon\text{Va}_{\text{Ni}}$ is a raw formation energy at the Ni site, E_0 is energy per atom in a perfect Ni_3Al, $\varepsilon\text{Ni}_{\text{Al}}$ is the raw formation energy of Ni on Al site (Ni anti-site), $\varepsilon\text{Ni}_{\text{Al}}$ is the raw formation energy of Al on Ni site (Al anti-site) and $b = 1/4$ [40,41].

The values of the formation energy at all three sites and the formation energy in the bulk are shown in Table 1. The reported values were obtained from two different *K*-point sampling and energy cutoffs. Both calculations are qualitatively consistent and it can be concluded that the formation energy in the bulk is higher than the vacancy formation energy at the other Ni sites. The calculations performed with higher *K*-point sampling and higher energy cutoff show the effective formation energy is higher in the bulk by approximately 0.05 eV.

It should be noted that values of the effective vacancy formation energy reported here are lower than those previously reported in experimental or theoretical studies, which indicate a value of 1.6 eV [41,42]. It is important to point out that our calculations were performed on large cells with limited *K*-point sampling in order to make the calculations feasible. These calculations are thus not expected to provide highly accurate absolute values. Nevertheless, the relative trends between the different configurations are expected to be valid.

5.6. Kinetics of the reordering

Finally, the reordering kinetics can be estimated from the knowledge of the activation energy (ΔQ) of the relevant diffusion steps. The activation energy for diffusion is determined as the addition of

Table 1
Vacancy formation energy in Ni_3Al two-layer complex stacking fault as estimated based on ab initio calculations.

Vacancy position	Vacancy formation energy (eV)	
	K-point [1 × 1 × 1], E_{cut} = 270 eV, fixed cell	*K*-point [1 × 2 × 1], E_{cut} = 351 eV, fixed cell
Va^{Ni}: Bulk	1.345	1.404
Va^{Ni}: Intrf(1 1 1)/Ni[1 1 0]	1.294	1.341
Va^{Ni}: Intrf(1 1 1)/Al^{Ni}[1 1 0]	1.314	1.368
Va^{Ni}: Cntr(1 1 1)/Ni[1 1 0]	1.378	1.346

migration and formation energies, $\Delta Q = \Delta G^{form} + \Delta G^{mig}$. As previously discussed, the most critical step of the reordering sequence is the first step. Thus, the activation energy of the entire sequence can be approximated with the value of the activation of the first step.

The present calculations reveal that the effective vacancy formation energy ΔG^{form} for the initial reordering sites is lower by approximately 0.05 eV than the in the bulk. The sites will thus have increased concentration of vacancies at the interface, and will promote the reordering kinetics.

The migration barrier ΔG^{mig} for the first step of the most likely exchange in the reordering sequence is ~0.93 eV. This value is about 0.07 eV higher than the migration barrier of 0.86 eV for the vacancy jump on the Ni sub-lattice in the "bulk" section of the super-cell. The higher value of the migration barrier of the first jump, as compared to the bulk, will have a retarding effect on the reordering kinetics.

Note that the calculated value of 0.86 eV for the migration barrier in the bulk of the super-cell is lower than the value of 0.97 eV reported in other ab initio work in the literature [43]. As mentioned above, this difference is due to limited *K*-point sampling and the relatively low energy cutoff 270 eV presently used. When the calculation are performed on $2 \times 2 \times 2$ Ni_3Al cell, with *K*-points sampling of $8 \times 8 \times 8$ and energy cutoff of 351 eV, the obtained migration barrier of 0.97 eV is fully consistent with the previous ab initio work in the literature [43].

Considering both contributions from ΔG^{form} to ΔG^{mig}, it is revealed that the differences are nearly mutually offset, which suggests that the activation energy for bulk and the first step in the reordering sequence are approximately the same. This is a very important result since it indicates that the reordering kinetics can be approximated using Ni self-diffusion in Ni_3Al.

This analysis represents a simplified picture for the kinetics of reordering. The simplifications are most notably that: (a) this analysis is based on the reordering of single pair of Al^{Ni} and Ni^{Al} anti-sites in a row of anti-sites. The single pair reordering eliminates two Al–Al nearest neighbors across the fault, but creates one Al–Al nearest neighbor bond in the central row, which is eliminated only upon subsequent reordering of the next anti-site pair. The energies associated with the vacancy exchanges will be altered for a partially-reordered fault. (b) This calculation accounts only for the activation energy (migration and formation), but not for correlation effects. (c) This analysis is based only on vacancy exchanges in a dislocation-free fault region, and does not consider the possible effect of the stress and strain field from the core of twinning partials. (d) Actual commercial alloys contains several alloying elements that are "γ′ formers" [44] that preferentially locate in the ordered precipitates and could modify the formation and migration energies that have been calculated above for binary Ni_3Al.

5.7. Reordering of other faulted structures

In the context of microtwining, it was shown that the reordering can proceed in the portion of microtwin that was created by an even number of identical $a/6\langle 1\,1\,2\rangle$ type dislocations. It is now useful to generalize the reordering condition in terms of the shear displacement with respect to {1 1 1} in $L1_2$ crystals. To fully avoid any Al–Al nearest neighbors, it is found that reordering can be accomplished only on faults that are formed by a net shear displacement of $n/3\langle 1\,1\,2\rangle$ or $n\langle 1\,1\,0\rangle$. In addition to the microtwinning mechanism described above, there are therefore several other dislocation mechanisms that meet the reordering criterion. Table 2 lists several possible dislocation configurations that create faults capable of reordering.

Configurations that do not meet the specified condition for reordering are also worthwhile examining. For example, one can imagine a situation in which a two-layer fault is created by two different partial dislocations, such as $a/6[1\,\bar{1}\,2]$ and $a/6[1\,2\,\bar{1}]$. The net displacement from these two dislocations is $a/6[2\,1\,1]$ and therefore the system is not capable of full reordering (SESF configuration). Nevertheless, this $2 \times$ CSF configuration can be partially reordered by reducing the number of Al–Al nearest neighbors in the central plane of the fault from two to one, which leads to a reduction of the fault energy.

Interestingly, a four-layer configuration created by a pair of $a/6[1\,\bar{1}\,2]$ and $a/6[1\,2\,\bar{1}]$ can be fully reordered. However, the complexity of the dislocation configuration and the fact that the full reordering can proceed only after passage of four dislocations may prevent such a shearing configuration and explain its absence in experimental observations.

Table 2
Example of sheared configurations capable of reordering.

Description	Schematic
Two 1/6⟨1 1 2⟩ on subsequent planes	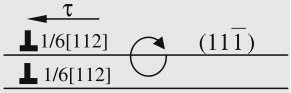
Two 1/6⟨1 1 2⟩ on separate planes	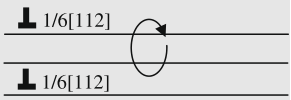
1/6⟨1 1 2⟩ and 1/2⟨1 1 0⟩ on subsequent planes	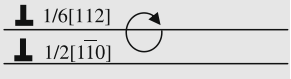
Zonal 1/6⟨1 1 2⟩ and 1/2⟨1 1 0⟩ on subsequent planes	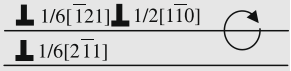
Two 1/2⟨1 1 0⟩ on subsequent planes	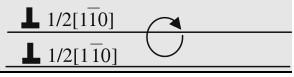

5.8. Implications for other mechanisms

The insights discussed above regarding reordering may also be key for understanding of a variety of other planar deformation mechanisms involving the shearing of γ′ precipitates that have been reported to operate at intermediate temperatures in Ni-based superalloys. Like microtwinning, these mechanisms also appear to progress in a viscous manner and be thermally activated [11,12,45].

One such a deformation mechanism involves the formation of "isolated" SESFs. In this mechanism, faulting (an SESF) occurs only in the γ′-phase [8,11,16]. The nature of the created faults implies that the matrix has been sheared by a perfect lattice translation, while the γ′-phase has been sheared by a pair of *a*/6[1 1 2] dislocations. The nature of γ′-phase shearing is identical to microtwinning, indicating that an identical diffusion-mediated reordering is also the rate-limiting process in this case.

The other most notable deformation mechanisms that do not rely on the operation of identical *a*/6[1 1 2] pairs, but nonetheless may require reordering, are: (a) the SISF mechanism that operates by *a*/3[1 1 2] dislocations and (b) the dislocation ribbon mechanism that operates by *a*[1 1 2] dislocations. Only the dislocation ribbon is further discussed in detail since the SISF mechanism can be considered as part of the dislocation ribbon mechanism, corresponding to the leading segment of the dislocation ribbon.

The dislocation ribbon mechanism operates under creep deformation conditions at approximately 750 °C and stresses 700–750 MPa during primary creep of single crystal alloys in near [1 0 0] orientation [12,46,47]. Such temperature and stress conditions are comparable to conditions that induce microtwinning in some microstructures of polycrystalline Rene 104 alloy. The identification of the dislocation ribbon and its recognition as the key deformation mechanism during primary creep was first made in series of publications by Kear et al. [12,46,48]. Their study was performed on Mar-M200, which can be considered a 1st generation superalloy. In subsequent studies on newer-generation superalloys, the operation of the dislocation ribbon has been confirmed and proposed as the dominant deformation process for primary creep of single crystals near [1 0 0] orientation [47].

The Burgers vector of the dislocation ribbon is *a*[1 1 2], which is a perfect translation in the $L1_2$ ordered crystal structure. The propagation of the dislocation thus does not leave planar defects in the γ/γ′ structure. However, the *a*[1 1 2] dislocation is widely spread and presents a configuration that can be distinguished by superlattice intrinsic/extrinsic stacking fault (SISF/SESF) ribbons. A schematic of the dislocation ribbon is shown in Fig. 15. The individual partial dislocation as well as the fault components of this configuration can be expressed as: *a*/3[1 1 2] and |SISF| and *a*/6[1 1 2] and |APB| and *a*/6[1 1 2] and |SESF| and *a*/3[1 1 2].

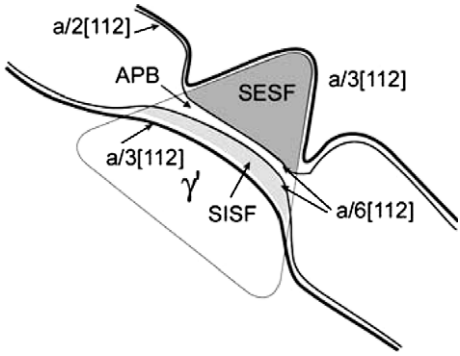

Fig. 15. Stacking fault ribbon reproduced from the work of Rae and Reed [47].

Although expressed differently, the previous work by Kear et al. [48,49] recognized that this deformation mechanism would be a viscous process limited by diffusion. As stated by Kear et al. [48] "the motion of the dislocation ribbon is most likely controlled by diffusion since adjustments are required at the core of the $a/3[1\ 1\ 2]$ leading dislocations as it enters the γ' particles". In the following text, we show that these adjustments are analogous to the reordering process, a fact that has not been recognized to date in the literature.

To understand the reordering or "adjustment" process, it is important to understand the dislocation configurations at the atomic level. In the early work of Kear et al. [49,50], it has been shown that there exist two different dislocation configurations with $a[1\ 1\ 2]$ Burgers vector that can produce the characteristic intrinsic/extrinsic fault. One of the dislocation configuration, which was subsequently found to be consistent with the experimental observations [12], is shown in Fig. 16. The configuration is complex, composed of a series of partial dislocations gliding on two adjacent planes. (The leading dislocation is on the left-hand side and the trailing is on the right-hand side). The detailed depiction of the dislocations is shown in Fig. 16a, while a compact notation is shown in Fig. 16b. In the compact notation, the leading $a/3[1\ 1\ 2]$ dislocation is represented as $\overline{\mathrm{B}\delta} + \mathrm{B}\delta$. Note that $\overline{\mathrm{B}\delta}$ is meant to imply

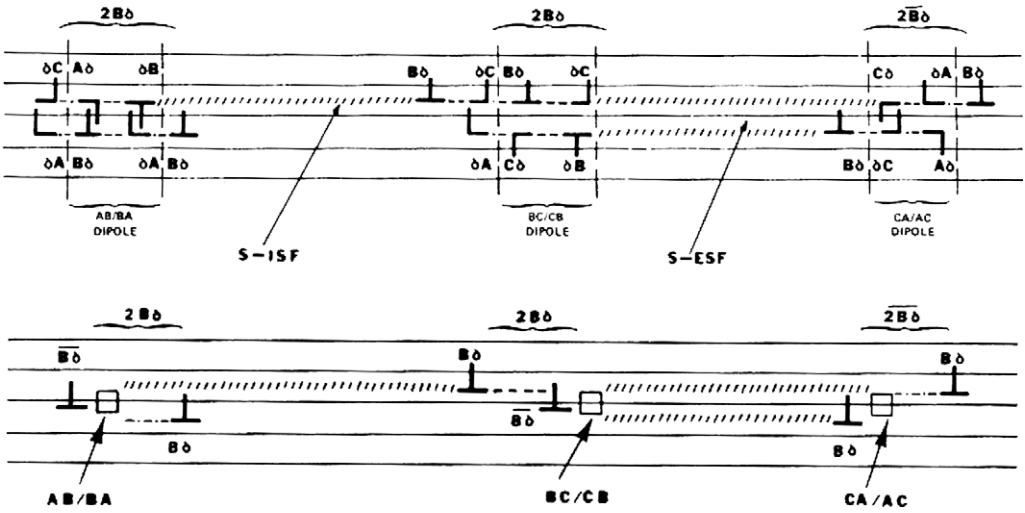

Fig. 16. The dislocation configuration in the intrinsic/extrinsic fault that is associated with the viscous slip. (a) The detail of the dislocation configuration and (b) simplified notation showing the dislocation dipole displacement [49].

that the dislocation is spread on two atomic planes (zonal dislocation), and is composed of a δC partial on one plane and a δA on the adjacent plane. Similarly, the second $a/6[1\,1\,2]$ partial is represented in equivalent way as $\overline{B}\overline{\delta}$.

The key components of the dislocation ribbon are the square symbols that indicate "dipole displacements." These dipole displacements provide the necessary shift of atoms in the central plane by $a/2\langle 1\,1\,0\rangle$ in order to obtain the low energy, Al–Al nearest-neighbor-free configuration in the wake of the gliding dislocations. There are three different dipole displacements required in the wake of the passing dislocations. Kear et al. [49] postulated that these dipole displacements are responsible for the propagation of the dislocation by viscous glide.

The interpretation given by Kear et al. [49] is directly analogous to reordering. However, their explanation must be modified with respect to the locations of the ordering/adjustments. This new interpretation is depicted in Figs. 17 and 18. Focusing on the first segment of the ribbon, which is shown in Fig. 17, it is recognized that reordering into an SISF can take place only after the passage of the entire $a/3[1\,1\,2]$. In other words, reordering can proceed only on the two-layer CSF(δC)/APB(BA) segment, but not on the two-layer CSF(δC)/CSF(δA) segment. The two-layer CSF(δC)/CSF(δA) could be partially reordered, but there are two degenerate states, only one of which converts to an SISF after the passage of the subsequent Bδ. It is not currently clear why there should be a bias towards a configuration that subsequently transforms to an SISF, and thus it is argued that the reordering can take place only at the core of the Bδ partial, or after its passage.

The reordering process of two-layer CSF(δC)/APB(BA) fault to an SISF is analogous to that described above for microtwinning. It requires a switch of atoms in the row of anti-sites. The row of anti-sites is along the AB/BA direction, as shown in Fig. 17e. Since the reordering atoms have a different bonding environment than microtwining, it is likely that activation barriers will be somewhat different than those calculated in Section 5.

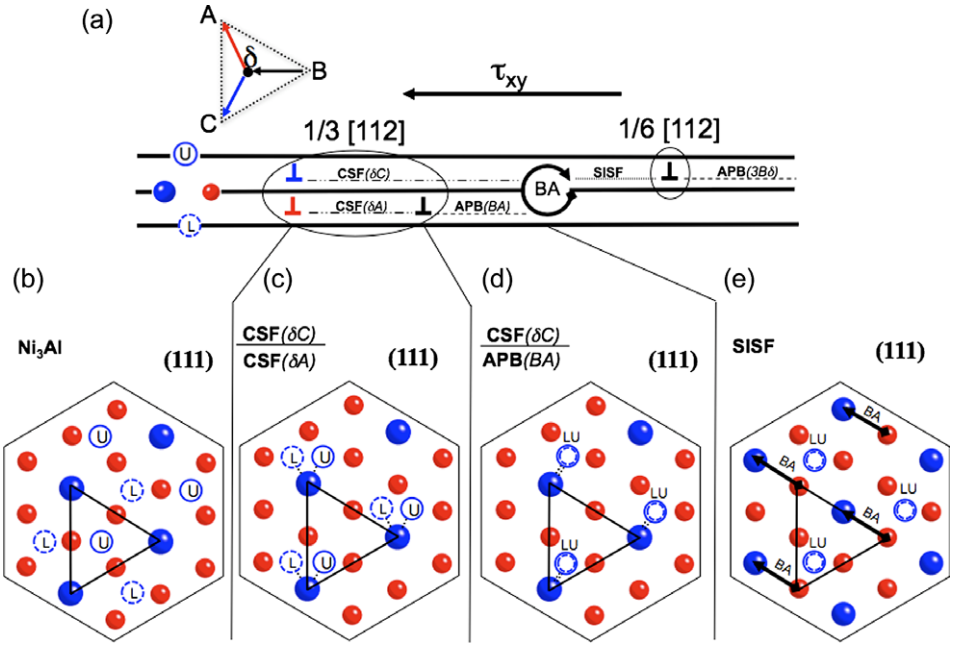

Fig. 17. (a) Edge-on schematic view of the leading $a/2[1\,1\,2]$ in the dislocation ribbon. The dislocation is split into a leading $1/3[1\,1\,2]$ and a trailing $1/6[1\,1\,2]$, which are separated by an SISF. (b–e) Plan-views of the atom arrangements for the three planes schematically shown in (a). For clarity, only Al atoms are shown for the upper (U) and the lower (L) plane in order to indicate the Al–Al nearest neighbor violations. The location where reordering must take place are indicated by the circular arrow. The atom color-coding is Ni-red "smaller", Al-blue "larger".

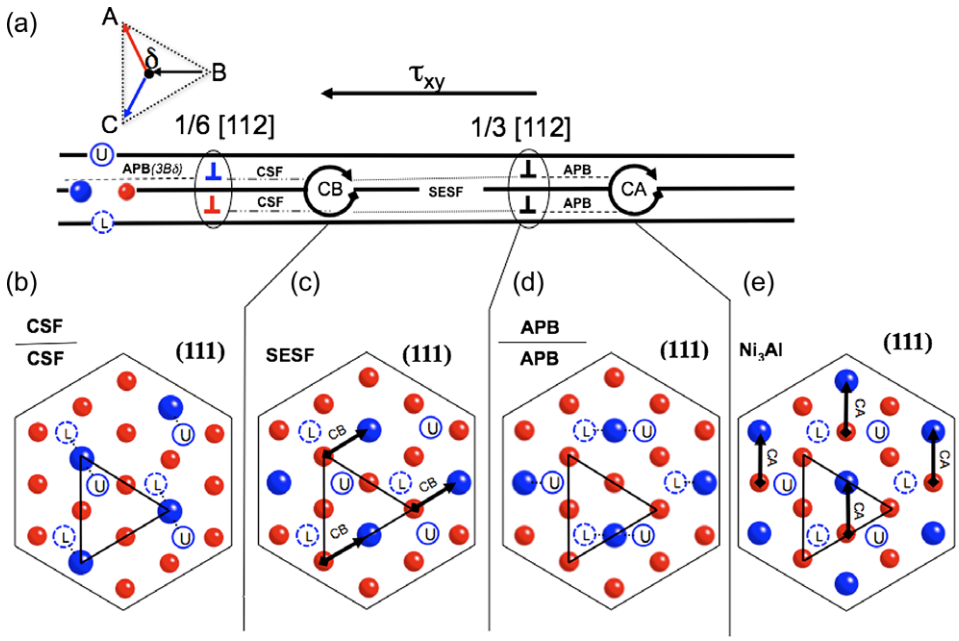

Fig. 18. (a) Edge-on schematic view of the trailing $a/2[1\,1\,2]$ in the dislocation ribbon. The dislocation is split into the leading $1/6[1\,1\,2]$ and trailing $1/3[1\,1\,2]$, both of which dislocations are separated by SESF. (b–e) Plan-views of the atom arrangements for the three planes schematically shown in (a). For clarity, only Al atoms are shown for the upper (U) and the lower (L) plane in order to indicate the Al–Al nearest neighbor violations. The two locations where reordering must take place are indicated by the circular arrow. The atom color-coding is Ni-red "smaller", Al-blue "larger".

A schematic of the dislocation components in the second segment of the dislocation ribbon, corresponding to $a/6[1\,1\,2]$, $a/3[1\,1\,2]$ and the coupling faults, is shown in Fig. 18. There are two separate locations where the diffusion-mediated reordering is required. One is at the core, or after the passage, of the zonal $a/6[1\,1\,2]$ partial, and converts the two-layer CSF into an SESF. The other is at the core, or after the passage of the $a/3[1\,1\,2]$ partial, and converts two-layer APB into perfect crystal. The reordering of 2-layer CSF to an SESF has the same activation barriers as previously described in Section 5.4. However, this is not the case for reordering of two-layer APB into perfect crystal. The bonding environment is different and thus different activation energies can be expected. The reordering can take place only after the passage of both $a/6[1\,1\,2]$ rather than after the first $a/6[1\,1\,2]$, as specified by Kear et al. [49].

The reordering concept provides a clear physical picture for understanding the dislocation ribbon movement. In this context, it becomes clear why all three dislocation segments have difficulty in propagating through the γ'-phase, a fact that is not well understood in the literature [47]. All three reordering processes proceed in a different bonding environment and thus it can be expected that they all will have different values for migration energy, and thus kinetics. It can be expected that the slowest reordering will dictate the motion of the ribbon. Further exploration of the energetics and kinetics for the two additional complex fault configurations identified for the stacking fault ribbon (in addition to the two-layer CSF explored in Section 5) will provide valuable insights into this shearing process.

The operation of an individual $a/3[1\,1\,2]$ super-Shockley partial dislocation is another important deformation mode at intermediate temperatures [27,45,51]. The individual $a/3[1\,1\,2]$ dislocation can be considered as a subset of the dislocation ribbon, which implies that reordering is also relevant for the creation of the SISF. This fact is not recognized in the literature. It is conventionally assumed that the SISF is created without the need for reordering [27]. This would indeed be the case if $a/3[1\,1\,2]$ dislocation moves in a compact core configuration or a single plane dissociated configuration. How-

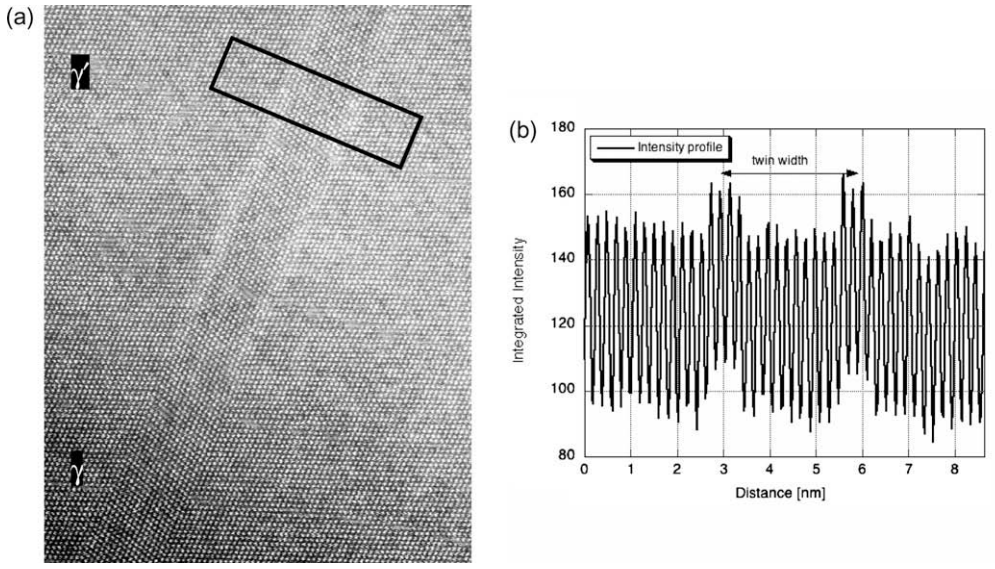

Fig. 19. (a) HAADF STEM image depicting a microtwin in γ/γ' interface. The image intensity is higher at the microtwin interface in γ' suggesting segregation of heavier elements. (b) Intensity profile obtained from a 2 nm wide region perpendicular to the interface.

ever, there exists both theoretical and experimental evidence indicating that $a/3[1\,1\,2]$ partial undergoes non-planar dissociation. Sun et al. [52] performed high-resolution TEM imaging which indicates a non-planar, spread dissociation. The non-planar dissociation of the $a/3[1\,1\,2]$ partial dislocation has been also discussed by Link [51]. An extrinsic fault at the head of the SISF was interpreted as the indication of non-planar spreading. The core structure of the $a/3[1\,1\,2]$ dislocation spread on two planes bounded by an SISF is also conceptually similar to what has been theoretically predicted by Yamaguchi et al. [53].

The non-planar spreading of the $a/3[1\,1\,2]$ has been previously considered as a locked configuration. Due to the original work by Giamei et al. [54], it is customary to refer to the configuration as a "Giamei lock". The locking indeed takes place at cryogenic temperature as discussed by Sun et al. [52] in the study of Ni_3Ga and Ni_3Al. However, at higher temperature and low strain rates, reordering becomes possible and may enable the glide of the spread configuration. Studies that establish the detailed aspect of the dislocation configuration for intermediate temperature shearing by $a/3[1\,1\,2]$ partials in Ni-based superalloys still needs to be undertaken.

6. Segregation at the microtwin interface

6.1. HAADF STEM observations

The HAADF STEM imaging reveals that reordering is not the only diffusion phenomenon associated with the formation of the microtwins. As shown in Fig. 19a, the microtwin interfacial region is often brighter in comparison to the bulk of the twin/surrounding matrix, which suggests segregation heavy elements. The fact that the enhanced intensity is likely to represent compositional variations from heavy elements is due to the nature HAADF imaging, where the intensity can be taken as proportional to the $Z^{\sim 1.7-2}$. The intensity profile in Fig. 19b shows that the intensity enhancement is detected in the interfacial plane and the adjacent (1 1 1) planes. The intensity profile was obtained as an average over 2 nm width of the profile box, as highlighted in Fig. 19a.

The enhanced intensity has been detected on many but not all the imaged microtwins. This indicates that the strength of the segregation can vary and is likely linked to the diffusion exposure time;

early forming microtwins would show higher intensity enhancement. The enhancement of the interfacial intensity is observed only in the γ′-phase portion of the microtwins, not in the γ matrix phase.

Detailed examination of the interfacial planes with the enhanced intensity often discloses the occurrence of periodic intensity variation along the length of the interface. Characteristic double period is detected in the planes. This can be well seen in the HAADF image shown in Fig. 20a, which depicts a presence of a two-layer fault. The periodic intensity variation could be best confirmed from a Fourier spectrum of the intensity profile, as shown in Fig. 20b. An extra peak at half reciprocal distance of the fundamental peak is indicative of the intensity variation. The FFT spectrum from the central (1 1 1) plane of the two-layer fault discloses a strong half peak. This is however not the case for the plane at the fault interface. The FFT spectrum from the adjacent planes on either side of the interface also shows presence of half period peak. The strength of the peak is smaller as compared to the central plane of the fault. Examination of the planes that are further away of from the interface does not reveal the presence of any similar periodic variation.

The intensity variation along the length of the interface suggests that the segregation is limited to one type of Ni_3Al sub-lattice site. The subtle superlattice contrast from (1 0 0) planes in the acquired images can be used as reference frame for the identification of the type of the sub-lattice. However, due to the complex composition of the γ′-phase in Rene 104, the scattering strength of the Ni

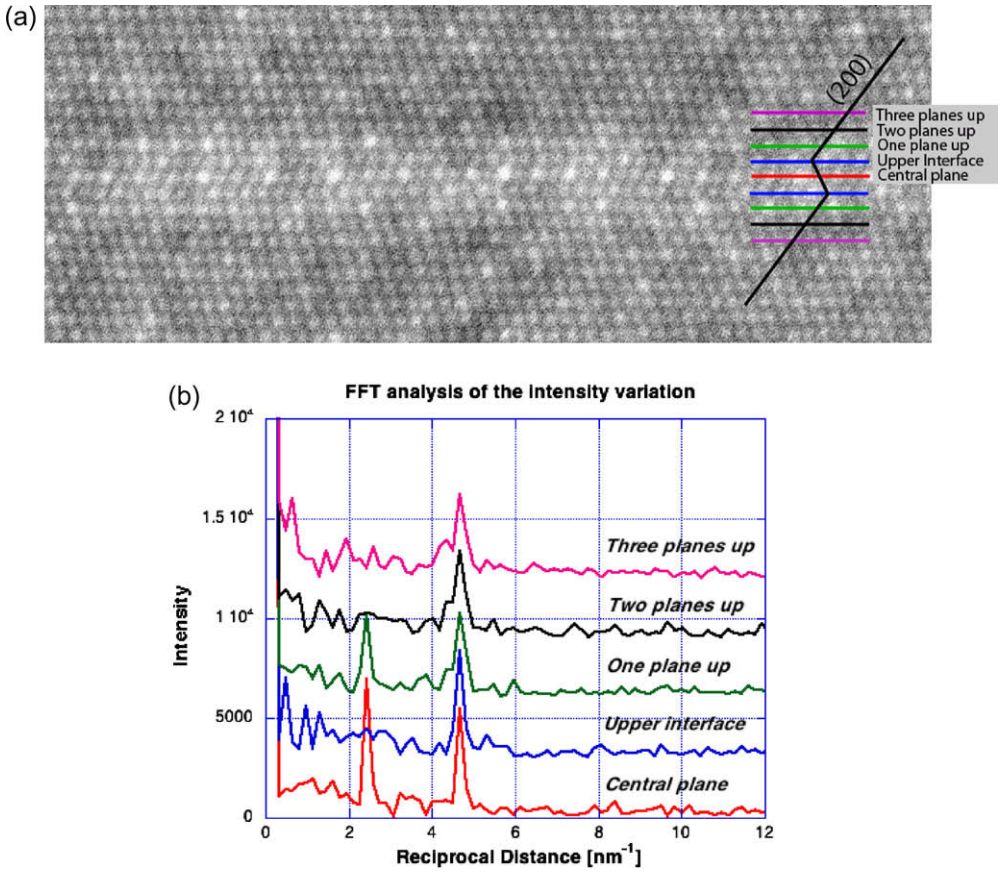

Fig. 20. (a) HAADF STEM image of a two-layer microtwin. (b) FFT spectra from intensity profiles taken along the length of the microtwin interface. Several profiles starting with the central plane and through the third plane from the interface were tested.

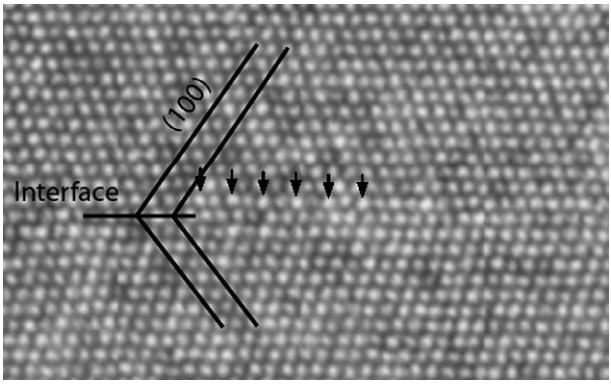

Fig. 21. HAADF STEM image of microtwin interface. The lower portion of the image is fourteen layer microtwin, the upper portion is surrounding γ′-phase. The planes adjacent to the microtwin interface display superlattice periodicity which is out of phase with the periodicity in the surrounding γ′, indicating that heavy elements are occupying Al sites in the plane adjacent to the microtwin interface.

(1 0 0) sub-lattice planes is not much stronger than the mixed Al–Ni (1 0 0) sub-lattice planes, and therefore the identification of the reference frame is very difficult in the as acquired image. An example of a microtwinned region where the distinction of the (1 0 0) planes can be recognized more clearly is shown in Fig. 21. The twinned region is the in the lower part of the image. The intensity modulation in the γ′ matrix in the upper part of the image is out of step with the intensity variation in the adjacent plane of the twin interface. This indicates that the heavy elements occupy the Al sites at the plane adjacent to the microtwin interface. More detailed analysis of the analysis will be presented elsewhere.

6.2. Site preference of elements in the γ′-phase

The presently available HAADF imaging provides a qualitative sense for the segregation of heavy elements to Al sub-lattice at the adjacent planes of the twin interface, although the identity of the elements has not yet been determined. Since the currently investigated alloy Rene 104 is a multi-elemental system, this could mean several different scenarios. Possible segregation scenarios consistent with the current observations are discussed in the context of the γ′-phase composition and the site-occupancy of the involved elements. Further experimental work, such as Atom Probe Tomography, EDX or EELS, which is currently not available, will need to substantiate the segregation scenario discussed below.

The nominal composition of the alloy and the composition of the γ′ and γ are shown in Table 3 [44,55]. For the purpose of segregation, it is important to focus on the elemental composition of the

Table 3
Nominal composition of Rene 104 [54]. The compositions of γ and γ′ (only secondary particles considered) from atom probe tomography technique [55].

Rene 104	Ni	Co	Cr	Al	Ti	Ta	B	C	Nb	Mo	W
Nominal (at.%)	Bal.	13.6–22.3	12.1–16.5	4.2–10.6	3.6–7.2	0.2–1.3	0.1–0.2	0.1–0.5	0.2–1.8	1.6–3.0	0.2–0.9
γ′ (at.%)	62.99	10.13	2.32	12.07	8.9	1.1	0.1	0.016	–	0.83	1.02
$\pm s_m$	0.18	0.12	0.05	0.20	0.11	0.04	0.04	0.02	–	0.03	0.10
γ (at.%)	34.77	28.36	27.8	2.63	0.82	0.209	0.11	0.029	–	3.30	1.08
$\pm s_m$	0.49	0.46	0.46	0.13	0.10	0.05	0.01	0.00	–	0.18	0.10

s_m: Standard error is calculated for elemental concentrations (c_i) with $s_m = \sqrt{c_i(1-c_i)/N_{TOT}}$, where N_{TOT} is the total number of atoms in the phase (γ or γ′).

γ′-phase and the site preference for the substitution elements, including Co, Cr, Ti, Ta, Nb, Mo and W, which are distributed between the two available sub-lattice sites (Al or Ni). The site-occupancy of the elements in the γ′-phase has been previously studied with experimental and theoretical approaches. The experimental measurement based on atom probe analysis has shown that Ti, Ta, W, Mo and Nb substitute for Al whereas Co substitutes for Ni [56,57]. The Cr can be shared between both sites in order to accommodate the stoichiometric balance [56]. The atom probe results are fully consistent with ab initio calculations for a substitution of single element into a binary Ni_3Al system. It was previously shown that Ti [58,59], Ta [59,60], Mo [58,61] and Nb [58] all prefer the Al sub-lattice while Co strongly prefers the Ni site [58,59]. There are contradictory reports concerning Cr site preference. The work by Jiang et al. [39] has shown that Cr prefers the Al site while the work of Suiter and Kawazoe [59] has shown that Cr has virtually no site preference.

The above analysis suggests that the HAADF experimental observations can be accounted for by segregation of heavy elements such as Ta, Mo, Nb, W from their Al sites in the bulk to the to Al sites in the interfacial region of the microtwins. Nevertheless, such a scenario needs to be substantiated by other experimental measurement, as it is also possible that a more complex rearrangement is taking place including chemical changes on the Ni sub-lattice site.

We have performed preliminary ab initio calculations that show that the elements such as Mo and Ta have a significant preference for the Al site in the central and adjacent planes of the two-layer twin (SESF). Interestingly, the opposite is true for two-layer complex fault. This suggests that such a segregation scenario could take place only after reordering. Detailed exploration of the segregation phenomenon is currently in progress.

6.3. Effect of segregation on dislocation mobility

The mobility of the twinning partials could be strongly affected by the presence of the heavy elements at the interface. One very obvious effect is through the strain field of the heavy atoms. The segregation appears to be enhanced on the {1 1 1} plane adjacent to the twin interface, which is the precise atomic plane on which the next twinning partial (of the subsequent pair) must move. Therefore, the observed segregation places heavy elements in the exact location to maximize their benefit for retarding the motion of the partials.

Another effect may be through the energy of the fault itself. The glide of two $1/6\langle 1\,1\,2\rangle$ partial dislocations on a pre-existing, reordered microtwin with segregation will cause the creation of CSF-like environment. This two-layer CSF-like structure is energetically less favorable in the presence of segregation. Thus, it can be expected that the higher fault energy can oppose the movement of the partials, decreasing the mobility of the dislocations. Finally, since the heavy elements are typically slow diffusers, the reordering reaction will possibly be slower. All of these potential effects must be explored in more detail in order to develop a more quantitative model of the influence of these alloying additions.

7. Influence of microstructure and applied stress on propensity for microtwinning

The scale of the precipitate structure and the relative volume fraction and size of the precipitates can be varied via cooling rate from above the γ′ solvus temperature (for supersolvus heat-treated materials), as well as by the subsequent aging treatment. The terminology adopted in the literature: the coarser precipitates are termed "secondary" while the finest population are termed "tertiary".

7.1. Effect of microstructure (cooling rate) on creep response

As exemplified in Fig. 22, the scale of the microstructure can have a significant effect on the creep rate. The corresponding energy-filtered TEM images [11] of the secondary and tertiary γ′ are shown in the insets. Shown in this figure are creep tests performed on Rene 88DT at 838 MPa and 650 °C for samples cooled at two different rates (secant cooling rates of 205 and 24 °C/s). The significant effect

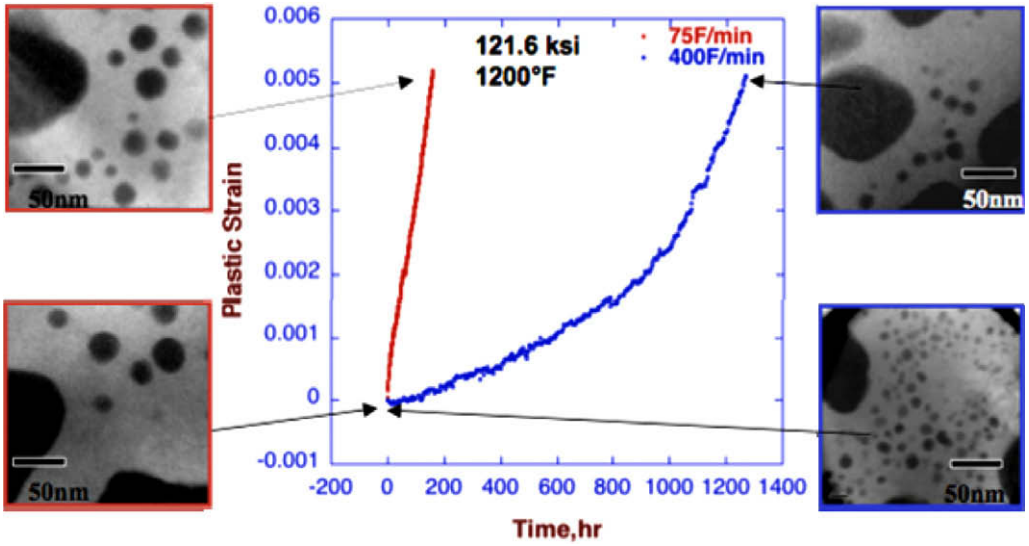

Fig. 22. Creep data for Rene 88 in two initial microstructural conditions (cooled at two different rates from the supersolvus temperature) showing the strong effect of tertiary volume fraction of creep strength. Coarsening of tertiary population occurs at these temperatures.

of microstructure on the creep response is apparent. Clearly, the shape of the curves, the overall strain rate and time to a given strain is strongly dependent on the initial microstructure. However, even more important is the recognition that the dominant deformation processes are also distinctly different in these specimens: isolated faulting of the secondary particles for the coarse microstructure and microtwinning for the fine microstructure, as shown in Fig. 23. The former deformation mode is characterized by $a/2[1\,1\,0]$ dislocation activity in the matrix, with apparent shearing of the secondary γ' precipitates by the presence of SESFs constrained to the particles (Fig. 23a). This deformation mode is contrasted with that in the finer, fast-cooled microstructure where the microtwinning process discussed above is predominant. In addition to this microstructure effect, there is also an effect of applied stress on deformation mechanism. For the fine microstructure, at higher stress (Fig. 23c), $a/2[1\,1\,0]$ dislocation loops are observed wrapping many of the secondary γ' precipitates, indicating that Orowan looping is prevalent. Remarkably, few if any microtwins are observed, as they are in this same microstructure at lower stress (Fig. 23b).

Insight into the microstructural factors affecting the transition from matrix dislocation activity to microtwinning have been obtained in recent experiments coupled with phase-field dislocation dynamics modeling [62]. These results are summarized presently. In order to explore the initiation of the microtwinning process in more detail, creep tests have been explored at small strain level. The substructure of a Rene 104 sample deformed to 0.05% plastic strain following deformation at 677 °C and 724 MPa is shown in Fig. 24. Under these deformation and microstructure conditions (fast cooling/fine microstructure), microtwinning is observed to be the dominant deformation process at 1 and 2% strain. However, at 0.05% plastic strain, a distinctly different substructure is observed. The matrix phase deforms first at this early stage of creep deformation. Fig. 24 shows $a/2\langle 1\,1\,0\rangle$ dislocations being emitted from an intergranular $M_{23}C_6$ carbide. Detailed dislocation analysis results show that these dislocations all have the same Burgers vector and that they have dissociated into Shockley partial dislocations that have a Burgers vector of the type $a/6\langle 1\,1\,2\rangle$. The leading partial dislocations appear to have "percolated" between the secondary γ' precipitates, leaving them unsheared. While the process whereby this structure subsequently evolves into microtwins is presently not clear, the decorrelation of $a/2[1\,1\,0]$ matrix dislocations nevertheless appears to be a necessary precursor to microtwinning.

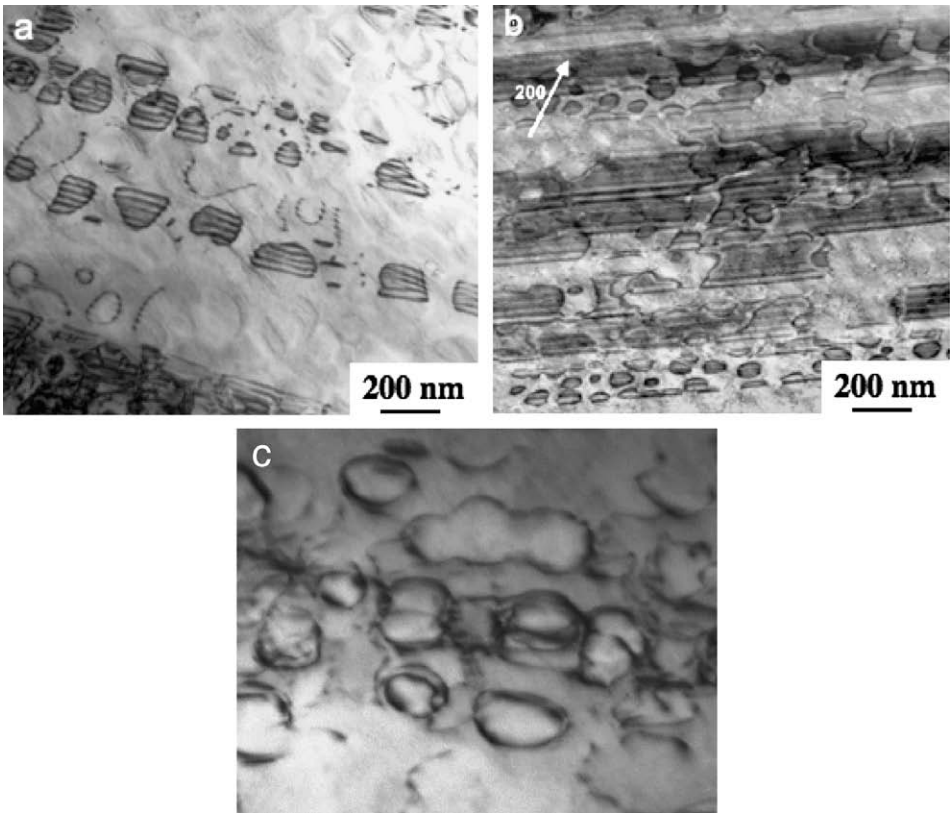

Fig. 23. Different deformation mechanisms in crept R88DT deformed at 650 °C. 838 MPa (a and b) and 976 MPa (c). (a) In the coarse microstructure at 838 MPa, isolated faulting is observed in which 1/2[1 1 0] dislocations are observed in the matrix while precipitates are sheared leaving SESFs. (b) In the fine microstructure at 838 MPa, microtwinning is dominant after 2% creep strain. (c) In the fine microstructure at 976 MPa, Orowan looping is observed.

7.2. Modeling of dislocation/precipitate interactions

There have been several simulation studies of the interaction of dislocations with precipitates for the superalloy structures. The early work of Mohles and Nembach [63] considered the propagation at strongly- and weakly-coupled $a/2\langle 1\,1\,0\rangle$ dislocations for the case of relatively low volume fraction γ' microstructures. More recent dislocation dynamics calculations by Rao et al. [64] further refined the modes of interactions and strength factors that can be derived from precipitate interactions. These simulations focused on APB shearing modes.

More recent simulations by Douin et al. [65] provided new insights into the role of the precipitate structure in promoting dissociation of matrix dislocations. In simulations similar to those of Douin et al [65], the interaction of $a/2\langle 1\,1\,0\rangle$ dislocation with precipitates and the various kinetic pathways associated with their dissociation have been explored using a different computational approach – the so-called microscopic phase-field (MPF) model [45]. The MPF enables treatment of complex shearing processes without any a priori assumptions about dislocation geometry, core structure, and formation of stacking faults [62, p. 42]. The model is an extension of the Peierls model of dislocation [66] with the incorporation of the generalized stacking fault (GSF) energy [67] and 3D anisotropic microelasticity theory [68]. It utilizes a description of dislocations in terms of shear type inelastic strain fields, which, combined with the voxel-to-voxel elastic interaction kernel, provides an efficient treatment for arbitrary dislocation geometries. The model stems from the phase-field dislocation model [60] and its

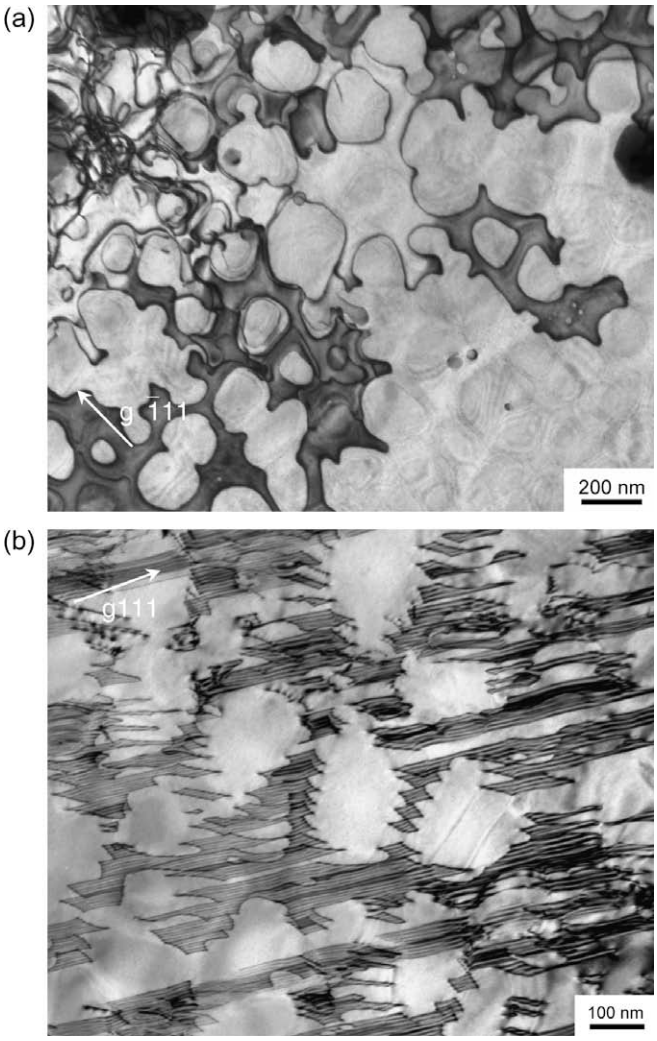

Fig. 24. Post creep dislocation substructure tested at 677 °C and 724 MPa and interrupted after (a) 0.05% strain showing $a/2\langle 1\ 1\ 0\rangle$ dislocation dissociation into Shockley partial dislocations bounding matrix intrinsic stacking faults and (b) 0.2% strain showing a high density of matrix intrinsic stacking faults resulting from the propagation of the leading Shockley partial dislocation.

modification [69] with a focus at the atomic length scales. With ab initio GSF energy, the MPF model is capable of treating dislocation core structures quantitatively. In addition, various planar faults are treated essentially as extended core structures and their formations are treated in a variational way. As applied to the study of dislocation activity in the γ/γ' microstructure, the MPF model is advantageous in handling both arbitrary configurations of dislocations and microstructure, dislocation curvatures, dislocation dissociation and stacking fault formation, anisotropic elastic interactions among dislocations and between dislocations and microstructure, and taking into account the more physical diffuse dislocation cores instead of singular (Volterra type) cores. As a result of the MPF studies, an understanding of the critical microstructure features and deformation conditions that favor microtwinning versus the various stacking faulting modes, will have important implications for the resultant creep strength.

A microscopic phase-field simulation was developed to study the experimentally observed $a/2\langle 1\,1\,0\rangle$ dislocation dissociation into Shockley partials since it is believed that this process is a precursor to the microtwinning mechanism as described in the preceding section. The simulation is based on a single screw-oriented dislocation as it interacts with a secondary γ' precipitate population with a size (diameter) of 300 nm and an interparticle spacing of 75 nm. A shear stress of 115 MPa acting on the dislocations in a direction parallel to the burgers vector of the leading Shockley partial Aδ (inset of Fig. 25) was used. The shear direction maximizes the force on the leading partial. Three configurations were initially chosen to show the feasibility of this model to capture the dissociation process and the results are presented in Fig. 25a–c for the same total simulation time. The first two cases where the intrinsic stacking fault energy was fixed at 10 mJ/m^2 for cases with and without tertiary γ' precipitates are presented in Fig. 25a–b.

In the phase-field model, starting with the case without tertiary γ precipitates, dissociation into Shockley partial dislocations occurs when the incoming dislocations come in contact with the narrow γ channel. As the applied stress is below the Orowan stress for the perfect dislocation (AB), it is suf-

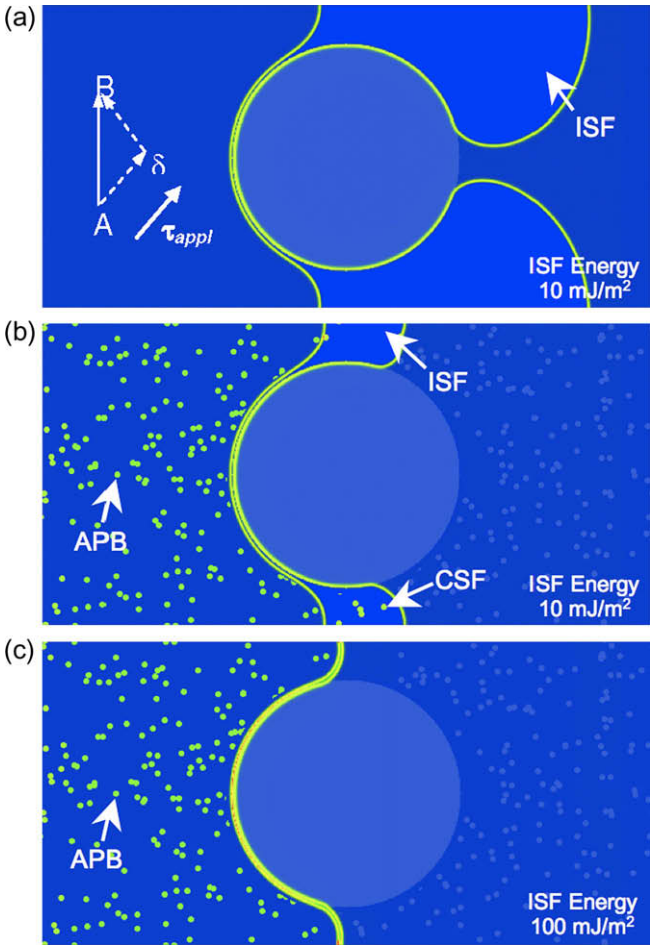

Fig. 25. Phase-field simulation of $a/2\langle 1\,1\,0\rangle$ dislocation (AB) interaction with an array of secondary γ' precipitates at an applied shear stress of 115 MPa, 300 nm γ' precipitate size, and 75 nm γ channel width spacing. The simulation shows the effect of tertiary γ' precipitates and stacking fault energy. (a) 10 mJ/m^2 ISF energy without tertiary γ', (b) 10 mJ/m^2 ISF energy w/tertiary γ' and (c) 100 mJ/m^2 ISF energy w/tertiary γ'. Periodic boundary condition is applied in the vertical direction.

ficient to drive the leading partial (Aδ) into the channel because of the smaller line tension (which is approximately proportional to b^2, where b is the Burgers vector of the partial). Note the stress resolved on the trailing partial is only half that on the leading partial for the orientation chosen. The leading Shockley sweeps out and creates an intrinsic stacking fault in the matrix while the trailing partial remains at the entrance to the γ channel. Similar results are observed when the simulation is run with a random distribution of tertiary γ′ precipitates (Fig. 25b), but in this case the presence of the tertiary γ′ offers an additional impediment to dislocation motion as APB′s are created in the wake of the passing $a/2\langle 1\,1\,0\rangle$ dislocation, and CSF′s are created in the tertiary γ′ after being sheared by the Shockley partial dislocations. For the same microstructure with tertiary γ′, but increasing the matrix stacking fault energy 10 fold to 100 mJ/m^2, leads to a quite different result, as shown in Fig. 25c. Under these circumstances, when the dislocation makes its way to the confines of the γ channel, due to the increase in matrix stacking fault energy, the dislocation does not dissociate into Shockley partials. Instead, the dislocation remains intact as a full $a/2\langle 1\,1\,0\rangle$ and is immobilized.

These preliminary results of the phase-field model demonstrate several important factors that trigger the decorrelation of the $a/2\langle 1\,1\,0\rangle$ dislocations, and leading ultimately to deformation via microtwinning. Several conclusions may be drawn at this point, and are summarized below:

(a) Not surprisingly, the matrix stacking fault energy is an important factor determining how the secondary γ′ particles are by-passed, and dictating the critical stress for by-pass. High fault energy inhibits decorrelation, and ultimately microtwinning.
(b) At a stress below the Orowan bowing stress for $a/2\langle 1\,1\,0\rangle$ dislocations (appropriately modified for frictional stresses or the presence of tertiary particles), decorrelation will be favored for microstructures in which the spacing between secondary particles is smaller. This rationale qualitatively explains the mechanism change for coarse and fine microstructures shown in Fig. 23a and b.
(c) If the stress is in excess of the Orowan bowing stress, then the matrix dislocations would remain undissociated, regardless of stacking fault energy. This argument is supported by the mechanism change noted in Fig. 23c. Note also that the absence of twins at this higher stress level would be difficult to understand if dislocation activity and microtwinning were operative in parallel. The phase-field simulations instead suggest that if the microstructure and stress conditions are favorable to $a/2\langle 1\,1\,0\rangle$ matrix activity, rather than decorrelation, then microtwinning will not be operative.
(d) The orientation of the applied shear stress relative to the operative Burgers vector should have a significant role on decorrelation. In the simulations shown in Fig. 25, the force acting on the leading partial is twice that acting on the trailing partial. If instead, the applied shear stress were oriented such that the trailing partial were more highly stressed, then decorrelation will not be favored. This indicates that decorrelation and microtwinning may only be favored over an relatively narrow range of applied shear stress orientation.

7.3. Subsequent formation of twins

The experimental evidence and modeling just described indicate that decorrelation of $a/2\langle 1\,1\,0\rangle$ dislocations is a necessary precursor to microtwinning. A detailed understanding of this progression remains the subject of investigation. Several possibilities are now briefly mentioned in light of the present understanding. A comprehensive review of deformation twinning has been provided by Christian and Mahajan [70]. For instance, many authors have proposed a pole mechanism to describe twinning in fcc crystals [71,72]. In these models, the common theme for the formation of a twin is the creation of a pole and twinning dislocation from a perfect $a/2\langle 1\,1\,0\rangle$ dislocation. The pole dislocation essentially acts as an anchor whereas the twinning dislocations ($a/6\langle 1\,1\,2\rangle$ Shockley partial dislocation) can sweep out on a {1 1 1} glide plane, rotating about a pole. There are opposing views concerning how twins form via a pole mechanism. This topic is beyond the scope of this paper and will not be detailed here [70].

In the model proposed by Mahajan and Chin [73], two co-planar $a/2\langle 1\ 1\ 0\rangle$ dislocations with different Burgers vectors are envisioned to react and form three identical Shockley partial dislocations on adjacent {1 1 1} glide planes, which can then act as the nucleus of a three layer twin. From the limited experimental evidence of microtwinning in the polycrystalline γ' strengthened superalloys investigated recently [11,17] all the $a/2\langle 1\ 1\ 0\rangle$ dislocations that are observed to dissociate into Shockley partial dislocations (e.g. see Fig. 24) have the same Burgers vector. This observation suggests that the microtwinning mechanism in these alloys differs from that proposed by Mahajan and Chin.

In the double cross-slip model originally proposed by Pirouz [74], a single screw-orientated $a/2\langle 1\ 1\ 0\rangle$ dislocation dissociates into two Shockley partial dislocations. Due to the larger shear stress acting on the leading Shockley partial dislocation, it will bow out in a manner reminiscent of a Frank-Read source and create an intrinsic stacking fault. When the leading Shockley partial re-combines with the static, trailing partial, the $a/2\langle 1\ 1\ 0\rangle$ dislocation that is once again created can cross-slip (along its screw orientation) by a single {1 1 1} plane, then re-dissociate into Shockley partial dislocations in the same manner as the dissociation on the initial {1 1 1} plane. If this operation were to be replicated on multiple, adjacent {1 1 1} planes, then Shockley partial dislocations possessing the same Burgers vector would now be operative and thus a microtwin could potentially develop. Based on the present, limited TEM evidence, it is not possible to definitively validate this mechanism. However, it is noted that this mechanism is consistent with the operation of single $a/2\langle 1\ 1\ 0\rangle$ slip systems as the source of the twins. Another, closely related process could be cross-slip and subsequent dissociation of $a/2\langle 1\ 1\ 0\rangle$ dislocations onto the intrinsic stacking faults in the matrix, present following decorrelation. This process would also create leading Shockley partial pairs of the same Burgers vector that could then cooperatively shear the larger γ' precipitates via the reordering process.

8. Conclusions

A summary of TEM studies of polycrystalline and single crystal Ni-based superalloys at intermediate temperatures (~650–750 °C) has been presented. There is a considerable variety of deformation mechanisms that have been reported following deformation in this regime. It is becoming increasingly clear that the mechanisms operative are dependent on details of microstructure, as well as the stress (or strain rate) and temperature.

While APB shearing of the γ' precipitates by coupled $a/2\langle 1\ 1\ 0\rangle$ dislocations is the predominant process at low temperatures, in this intermediate temperature regime, other shearing modes become active, including the formation of SESFs and microtwins. These mechanisms have been observed at relatively low stress levels, below the yield strength, and appear to depend strongly on temperature. These are particularly unusual characteristics for deformation twinning in general, and the thermally-activated nature of this mechanism in the superalloys is linked to the diffusion-mediated reordering of the ordered structure within the precipitates after being sheared by the $a/6\langle 1\ 1\ 2\rangle$ twinning partials. The reordering process removes wrong nearest neighbors at the complex stacking faults created by pairs of twinning partials acting on adjacent {1 1 1} planes. Reordering enables pairs of $a/6\langle 1\ 1\ 2\rangle$ partials to shear the secondary γ' particles at modest stress levels – a process not possible in the absence of reordering. Detailed analysis of the atomic steps of reordering by first principles calculations coupled with the nudged elastic band method suggests that the activation energy for reordering should be similar to that for Ni self-diffusion in the bulk, under the simplifying assumption of ordered Ni_3Al being representative of the γ' precipitate composition.

An important conclusion from the present knowledge of the mechanisms that depend on reordering is that they may initiate at temperatures that are lower than those required for general climb of dislocations. Reordering is a conservative process involving diffusion distances of atomic dimensions, while climb by-pass requires long-range diffusion over distances comparable to the precipitate size. Therefore, these novel shearing processes may be relevant to the detailed understanding and potential future application of this class of alloys since they are responsible for the transition from the lower temperature, relatively rate-independent deformation, to the higher temperature, rate-dependent processes.

Finally, the observation of segregation of heavy elements at the fault and twin planes within the γ' particles indicates that this feature is closely related to the reordering process. The elements involved

in the segregation have not yet been determined, but their presence may be vitally important in promoting faulting and twinning in these systems, as well as moderating the rate of creep through potent interaction with the twinning partials.

Acknowledgement

This work has been supported by US Air Force Office of Scientific Research under the MEANS 2 program Grant No. FA9550-05-1-0135.

References

[1] Gleiter H, Hornbogen E. Phys Status Solidi 1965;12:251.
[2] Gleiter H, Hornbogen E. Mater Sci Eng 1968;2:285.
[3] Sun YQ, Hazzledine PM. Philos Mag 1988;58:603.
[4] Kozar RW, Suzuki A, Milligan WW, Schirra JJ, Savage MF, Pollock TM. Metall Trans A, in press.
[5] Manonukal A, Dunne FPE, Knowles D. Acta Mater 2002;50:2917.
[6] Arzt E, Rosler J. Acta Metall 1988;36:1053.
[7] Rosler J, Arzt E. Acta Metall Mater 1990;38:671.
[8] Decamps B, Rajoul S, Coujou A, Pettinari-Sturmel F, Clement N, Locq D, et al. Philos Mag 2004;84:91.
[9] Chen QZ, Knowles DM. Mater Sci Eng A 2003;356:352.
[10] Milligan WW, Antolovich SD. Metall Trans A: Phys Metall Mater Sci 1991;22A:2309.
[11] Viswanathan GB, Sarosi PM, Henry MF, Whitis DD, Milligan WW, Mills MJ. Acta Mater 2005;53:3041.
[12] Kear BH, Leverant GR, Oblak JM. Trans ASM 1969;62:639.
[13] Foreman AJE, Makin MJ. Philos Mag A 1966;14:911.
[14] Unocic RR, Viswanathan GB, Sarosi PM, Karthikeyan S, Li S, Mills MJ. Mater Sci Eng, A 2008:483–484:25.
[15] Kolbe M. Mater Sci Eng 2001;319–321:383.
[16] Viswanathan GB, Karthikeyan S, Sarosi PM, Unocic RR, Mills MJ. Philos Mag 2006;86:4823.
[17] Unocic RR, Kovarik L, Sarosi PM, Mills MJ. in preparation.
[18] Legros M, Clement N, Caron P, Coujou A. Mater Sci Eng 2002;A337:160.
[19] Pollock TM, Argon AS. Acta Metall Mater 1994;42:1859.
[20] Pollock TM, Field RD. Dislocations and high temperature plastic deformation of superalloys single crystal. In: Nabarro FRN, Duesbery MS, Hirth J, editors. Dislocations in solids. Elsevier; 2002.
[21] Kear BH, Oblak JM. J Phys 1974;12:c7.
[22] Kear BH, Oblak JM, Giamei F. Slip, viscous slip and climb processes in g′ precipitation hardened nickel-base alloys. In: ICSMA 2; 1970. p. 1155.
[23] Kakehi K, Sakaki T, Gui JM, Misaki Y. In: Willshire B, Evans RW, editors. Proceedings of the 5th international conference on creep and fracture of engineering materials and structures; 1993. p. 221.
[24] Kuttner T, Feller-Kniepmeier M. J Phys IV: Proc 1993;3:325.
[25] Ardakani MG, McLean M, Shollock BA. Acta Mater 1999;47:2593.
[26] Guimier A, Strudel JL. Stacking fault formation and mechanical twinning processes in a nickel-base superalloy during tensile deformation at high temperature. In: Proceedings of the 2nd international conference on strength of metals and alloys. OH: ASM Metals Park; 1970. p. 1145.
[27] Knowles DM, Chen QZ. Mater Sci Eng 2003;A340:88.
[28] Kolbe M, Pelissier M, Ignat B, Schollock B, McLean M, Dupeux M, et al. High temperature high voltage electron microscope in situ observation of deformation mechanisms in single crystal superalloys. In: Proceedings of the 10th international conference on strength of materials: fundamental physical aspects of the strength of crystalline materials. Sendai: Japan Institute of Metals; 1994. p. 685.
[29] Sarosi PM, Viswanathan GB, Mills MJ. Scripta Mater 2006;55:727.
[30] Li J. Model Simul Mater Sci Eng 2003;11:173.
[31] Karthikeyan S, Unocic RR, Sarosi PM, Viswanathan GB, Whitis DD, Mills MJ. Scripta Mater 2006;54:1157.
[32] Kresse G, Furthmüller J. Phys Rev B 1996;54:11169.
[33] Kresse G, Furthmüller J. Comput Mater Sci 1996;6:15.
[34] Kresse G, Hafner J. Phys Rev B 1994;49:14251.
[35] Kresse G, Hafner J. J Phys: Condens Matter 1994;6:8245.
[36] Kresse G, Joubert D. Phys Rev B 1999;59:1758.
[37] Henkelman G, Uberuaga BP, Jonsson H. J Chem Phys 2000;113:9901.
[38] Harris C, Tedstrom R, Daw MS, Mills MJ. Comput Mater Sci 2006;37:462.
[39] Jiang C, Sordelet DJ, Gleeson B. Acta Mater 2006;54:1147.
[40] Mishin Y. Acta Mater 2000;48:589.
[41] Mishin Y. Acta Mater 2004;52:1451.
[42] Wang T, Shimotomai M, Doyama M. J Phys F: Metal Phys 1984;14:37.
[43] Zhang X, Wang C-Y. Acta Mater 2009;57:224.
[44] Mourer DP, Williams JL. Dual heat treat process development for advanced disk applications. In: Greem KA, Pollock TM, Harada H, Howson TE, Reed RC, Schirra JJ, et al., editors. Superalloys 2004. TMS (The Minerals, Metals & Materials Society); 2004. p. 401.

[45] Unocic RR, Kovarik L, Shen C, Sarosi PM, Wang Y, Li J, et al. Deformation mechanisms in Ni-base disk superalloys at higher temperatures. In: Reed RC, Green A, Caron P, Gabb TP, Fahrmann MG, Huron ES, et al., editors. Superalloys 2008. TMS; 2008. p. 377.
[46] Leverant GR, Kear BH. Metall Trans 1970;1:491.
[47] Rae CMF, Reed RC. Acta Mater 2007;55:1067.
[48] Kear BH, Oblak JM, Giamei A. Metall Trans 1970;1:2477.
[49] Kear BH, Giamei A, Leverant GR, Oblak JM. Scripta Mater 1969;3:455.
[50] Kear BH, Giamei A, Leverant GR, Oblak JM. Scripta Mater 1969;3:123.
[51] Link T. Scripta Metall Mater 1994;31:671.
[52] Sun YQ, Crimp MA, Hazzleidine PM. Philos Mag A 1991;64:223.
[53] Yamaguchi M, Paidar V, Pope DP, Vitek V. Philos Mag A 1982;45:867.
[54] Giamei A, Oblak JM, Kear BH, Rand WH. In: 29th Annual meeting EMSA. Baton Rouge: Claitor's Publ.; 1971. p. 112.
[55] Sarosi PM, Miller MK, Isheim D, Mills MJ. in preparation.
[56] Blavette D, Cadel E, Deconihout B. Mater Charact 2000;44:133.
[57] Miller MK, Jayram R, Lin LS, Cetel AD. Appl Surf Sci 1994;76–77:172.
[58] Yang J, Xiao CY, Xia SD, Wang KL. J Phys: Condens Matter 1993;5:6653.
[59] Sluiter MHF, Kawazoe Y. Phys Rev B 1995;51:4062.
[60] Wang YU, Jin YM, Cuitino AM, Khachaturyan AG. Acta Mater 2001;49:1847.
[61] Geng CY, Wang CY, Yu T. Acta Mater 2004;52:5427.
[62] Shen C, Li J, Mills MJ, Wang Y. Modeling shearing of g′ in Ni-base superalloys. In: Gunter G, editor. Integral materials modeling: towards physics based through-process models. Weinheim: Wiley-VCH Verlag GmbH & Co. KGaA; 2007. p. 243.
[63] Mohles V, Nembach E. Acta Mater 2001;49:2405.
[64] Rao SI, Parthasarathy A, Dimiduk DM, Hazzledine PM. Philos Mag A 2004;21:3195.
[65] Douin J, Pettinari-Sturmel F, Coujou A. Acta Mater 2007;55:6453.
[66] Peierls RE. Proc Phys Soc 1940;52:34.
[67] Vitek V. Philos Mag 1968;18:773.
[68] Khachaturyan AG. Theory of structural transformations in solids. New York: John Wiley & Sons; 1983.
[69] Shen C, Wang Y. Acta Mater 2003;51:2595.
[70] Christian JW, Mahajan S. Prog Mater Sci 1995;39:1.
[71] Sleeswyk AW. Philos Mag 1974;29:407.
[72] Venables JA. Philos Mag 1961;6:379.
[73] Mahajan S, Chin GY. Acta Metall 1973;21:1353.
[74] Pirouz P. Scripta Metall 1987;21:1463.